

Towards the phase diagram of dense two-color matter

Seamus Cotter,¹ Pietro Giudice,² Simon Hands,² and Jon-Ivar Skullerud^{1,3}

¹ *Department of Mathematical Physics, National University of Ireland Maynooth, Maynooth, County Kildare, Ireland.*

² *Department of Physics, College of Science, Swansea University, Singleton Park, Swansea SA2 8PP, U.K.*

³ *Institute for Nuclear Theory, University of Washington, Seattle, WA 98195–1550, USA.*

We study two-color QCD with two flavors of Wilson fermion as a function of quark chemical potential μ and temperature T . We find evidence of a superfluid phase at intermediate μ and low T where the quark number density and diquark condensate are both very well described by a Fermi sphere of nearly-free quarks disrupted by a BCS condensate. Our results suggest that the quark contribution to the energy density is negative (and balanced by a positive gauge contribution), although this result is highly sensitive to details of the energy renormalisation. We also find evidence that the chiral condensate in this region vanishes in the massless limit. This region gives way to a region of deconfined quark matter at higher T and μ , with the deconfinement temperature, determined from the renormalised Polyakov loop, decreasing only very slowly with increasing chemical potential. The quark number susceptibility χ_q does not exhibit any qualitative change at the deconfinement transition. We argue that this is because χ_q is not an appropriate measure of deconfinement for 2-color QCD at high density.

I. INTRODUCTION

Despite over a decade of intensive efforts to unveil the phase structure of strongly interacting matter at high density (beyond a few times the nuclear saturation density) and low temperature, even the question of which phases exist remains unanswered. A quantitative knowledge of this region would allow us to answer many questions regarding the structure and properties of compact stars, including the question of whether deconfined quark matter can exist inside such stars. The reason for the lack of definite progress on this issue is that standard weak-coupling methods are inapplicable except at asymptotically high densities, while the various model approaches that have been employed have not been sufficiently constrained by input from experiment or first-principles theoretical calculations to yield reliable information in the region of interest. Thus, while a wealth of information exists regarding possible phases and their properties in various models, no reliable, quantitative results are available as yet. For a recent review of high-density QCD, see Ref. [1].

Many of the outstanding questions could in principle be answered by lattice QCD simulations, but these have been hindered by the notorious sign problem. While no method has as yet been shown to solve the sign problem for QCD, lattice simulations may still constrain model calculations by providing first-principles, nonperturbative results for QCD-like theories without a sign problem. This is the main aim of the present study.

Among these theories, QCD with gauge group $SU(2)$ (two-color QCD or QC_2D) is of particular interest in that it shares most of the salient features of real QCD (eg, confinement, dynamical chiral symmetry breaking and long-range interactions). It differs from QCD in that the baryons of the theory are bosons, and the lightest baryon is a pseudo-Goldstone boson, degenerate with the pion (note though, that $SU(2)$ models with adjoint matter [2] and G_2 with fundamental matter [3], both of

which are free from a sign problem, are expected to contain fermionic baryons in the physical spectrum). Therefore, instead of a normal nuclear matter phase this theory has a superfluid state characterised by condensation of these baryons, which at this point become true Goldstone bosons. This has been observed in a number of lattice simulations; in particular, the excitation spectrum including the Goldstone bosons has been studied in Refs. [4, 5]. A transition to a state of deconfined quark matter is expected at high chemical potential μ (see however [6]), and evidence of this was found in [7, 8]. The precise nature of this transition remained unclear, however, and in this paper we will attempt to answer some of the outstanding questions about this.

An intriguing possibility is that in an intermediate régime, strongly interacting matter may enter a chirally symmetric and confined phase, dubbed *quarkyonic* [9]. In [8], it was suggested that the scaling of thermodynamic quantities with μ in the intermediate régime could be a sign of such a phase. It was not possible to draw any further conclusions, not least because the presence of a non-zero diquark source $j \neq 0$, introduced to stabilise the simulations, distorted the μ -dependence of the relevant quantities. This will be remedied in the present paper.

This paper is organised as follows. In Section II we present results from simulations at zero chemical potential. These results allow us to map out lines of constant physics, including the line of zero quark mass, which will in the future allow us to perform controlled extrapolations to the continuum and chiral limits, and also by varying N_τ at fixed cutoff to estimate the critical temperature T_d for deconfinement at $\mu = 0$. In addition, these results form a large part of the input into the renormalisation of energy densities, which is described and carried out in Section III. Section IV contains the bulk of our results for the (μ, T) phase diagram. After addressing some general technical issues in Section IV A, we present in Section IV B results for the order parameters for superfluidity and deconfinement, giving us an

β	κ	N_s	N_τ	N_{traj}	am_π	m_π/m_ρ	a (fm)
1.7	0.1780	12	24	500	0.779(7)	0.804(10)	0.229(3)
1.7	0.1790	12	24	1050	0.683(5)	0.783(12)	0.213(8)
1.7	0.1810	12	24	500	0.438(15)	0.61(5)	0.189(4)
1.8	0.1740	12	24	2000	0.640(4)	0.778(7)	0.178(8)
1.8	0.1750	12	24	880	0.490(9)	0.67(2)	0.174(8)
1.9	0.1680	12	24	1570	0.645(8)	0.805(9)	0.178(6)
1.9	0.1685	12	24	2000	0.589(4)	0.780(9)	0.153(18)
1.9	0.1690	12	24	1000	0.517(11)	0.71(2)	0.144(8)
2.0	0.1620	12	24	1000	0.638(7)	0.830(9)	0.164(5)
2.0	0.1625	16	32	2000	0.586(3)	0.820(8)	
2.0	0.1627	16	32	2000	0.562(4)	0.809(8)	
2.0	0.1630	12	24	1000	0.524(10)	0.758(16)	0.145(3)
		16	32	2000	0.508(4)	0.785(9)	
2.1	0.1570	16	32	1600	0.536(3)	0.836(8)	
2.1	0.1580	16	32	2100	0.405(5)	0.770(12)	

TABLE I: Simulation parameters, pi and rho masses and lattice spacing at $\mu = j = 0$.

outline of the (μ, T) phase diagram. Section IV C contains results for the thermodynamic quantities, baryon density and (renormalised) energy density, while Section IV D contains results for the quark number susceptibility (preliminary results from this work were presented in Ref. [10]), and in Section IV E we investigate chiral symmetry breaking and restoration. Finally, in Section V we summarise our results and their implications.

II. SIMULATION DETAILS AND VACUUM PHASE STRUCTURE

We study QC₂D with a conventional Wilson action for the gauge fields and two flavours of Wilson fermion. The fermion action is augmented by a gauge- and iso-singlet diquark source term which serves the dual purpose of lifting the low-lying eigenvalues of the Dirac operator and allowing a controlled study of diquark condensation. The quark action is

$$S_Q + S_J = \sum_{i=1,2} \bar{\psi}_i M \psi_i + \kappa j [\psi_2^{tr} (C\gamma_5)\tau_2 \psi_1 - h.c.], \quad (1)$$

with

$$M_{xy} = \delta_{xy} - \kappa \sum_{\nu} \left[(1 - \gamma_{\nu}) e^{\mu\delta_{\nu 0}} U_{\nu}(x) \delta_{y, x+\hat{\nu}} + (1 + \gamma_{\nu}) e^{-\mu\delta_{\nu 0}} U_{\nu}^{\dagger}(y) \delta_{y, x-\hat{\nu}} \right]. \quad (2)$$

Further details about the action and the Hybrid Monte Carlo algorithm used can be found in [7].

We have performed an extensive exploration of the parameter space in the vacuum ($T = \mu = j = 0$) in the range $\beta = 1.7 - 2.1$. The parameters used are shown in Table I, together with the values obtained for the pion

β	1.7	1.8	1.9	2.0	2.1
κ_c	0.18226_{-8}^{+8}	0.17644_{-11}^{+15}	0.17089_{-19}^{+20}	0.16456_{-10}^{+14}	0.15935_{-8}^{+8}

TABLE II: Critical hopping parameter κ_c given by $m_\pi^2(\kappa_c) = 0$, for different values of β .

(pseudoscalar meson) mass m_π , ratio of pion to rho (vector meson) mass m_π/m_ρ and lattice spacing a . The lattice spacing was determined by fitting the static quark potential to the Cornell form $V(r) = C + \alpha/r + \sigma r$ and taking the string tension to be $\sqrt{\sigma} = 440\text{MeV}$.

We can determine the value $\kappa_c(\beta)$ where the quark mass vanishes by performing a linear extrapolation of m_π^2 in $1/\kappa$ for each value of β . The results of this are shown in Table II.

We have also investigated the thermal deconfinement transition at $\mu = 0$ using the fixed-scale approach. We have generated configurations with $N_\tau = 4 - 10$ at $\beta = 1.9, \kappa = 0.168$, corresponding to a temperature range of 113–281 MeV. At each temperature we have computed the Polyakov loop $\langle L \rangle$, which is an order parameter for deconfinement of static color charges in the pure gauge theory, and exhibits a rapid crossover in a theory with dynamical fermions. It is related to the free energy F_q of a static quark by

$$L = e^{-F_q(T)/T}. \quad (3)$$

The free energy F_q is only defined up to an additive renormalisation constant ΔF , which depends on the bare couplings β, κ . Different prescriptions for determining this constant correspond to different renormalisation schemes. We have imposed the condition that the renormalised Polyakov loop on our $N_\tau = 4$ lattice ($T = 263$ MeV) is equal to 1, or in other words, the free energy is zero at this temperature. We can then compute the renormalised Polyakov loop $L_R(T)$ at any other temperature T from the bare Polyakov loop L_0 via

$$\begin{aligned} L_R(T) &= e^{-F_R(T)/T} = e^{-(F_0(T)+\Delta F)/T} \\ &= L_0(T) e^{-\Delta F/T} = Z_L^{N_\tau} L_0(T = 1/aN_\tau), \end{aligned} \quad (4)$$

where $Z_L = \exp(-a\Delta F) = L_0(N_\tau = 4)^{-1/4}$ (this procedure was first outlined in Ref. [11]). The results are shown in Fig. 1, as a function of $aT = 1/N_\tau$. The red (solid) curve in Fig. 1 is a cubic spline interpolation between the data points. Taking the derivative of this (denoted by the green, dashed curve), we find the maximum at $Ta = 0.193$. If we instead use an Akima spline to interpolate, the maximum of the derivative appears at $Ta = 0.183$. Taking the cubic spline as our best estimate and conservatively estimating the uncertainty to be twice the difference between the Akima and cubic spline estimates, our result for the deconfinement temperature is $T_d(\mu = 0)$ is $T_d a = 0.193(20)$ or $T_d = 217(23)$ MeV.

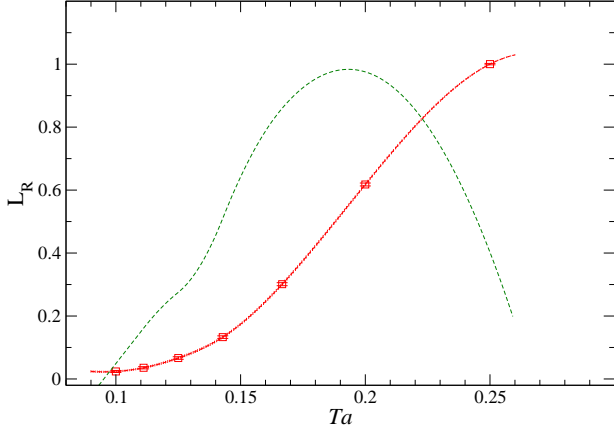


FIG. 1: The renormalised Polyakov loop L_R as a function of temperature T , for $16^3 \times N_\tau$ lattices at $\beta = 1.9, \kappa = 0.168, \mu = j = 0$. The red (solid) band is a cubic spline interpolation between the data points, and the green (dashed) curve shows the derivative of the interpolation curve, divided by a factor of 10.

III. RENORMALISATION OF ENERGY DENSITIES

To determine the energy density, it is convenient to introduce different lattice spacings a_s, a_τ in the space and time directions, with an anisotropy parameter $\xi \equiv a_s/a_\tau$. The energy density ε is then given by [12, sec. 5.4.1]

$$\varepsilon(T) = -\frac{1}{V} \frac{\partial Z}{\partial T^{-1}} \Big|_V = -\frac{\xi}{N_s^3 N_\tau a_s^3 a_\tau} \left\langle \frac{\partial S}{\partial \xi} \Big|_{a_s} \right\rangle, \quad (5)$$

where we have used $V = (N_s a_s)^3, T^{-1} = N_\tau a_\tau$, and

$$\frac{\partial}{\partial a_\tau} \Big|_{a_s} = -\frac{a_s}{a_\tau^2} \frac{\partial}{\partial \xi} \Big|_{a_s}. \quad (6)$$

The partial derivatives must be taken with all other physical parameters kept fixed. In our case, this means that the physical quark mass, and therefore the ratio m_π/m_ρ , is kept fixed.

The anisotropic action $S = S_G + S_Q + S_J$ describing $N_f = 2$ Wilson quark flavors is given by

$$S_G = -\frac{\beta}{N_c} \left[\frac{1}{\gamma_g} \sum_{x,i < j} \text{Re Tr } U_{ij}(x) + \gamma_g \sum_{xi} \text{Re Tr } U_{i0}(x) \right], \quad (7)$$

$$S_Q = \sum_{x,\alpha} \left[\bar{\psi}^\alpha(x) \psi^\alpha(x) + \gamma_q \kappa \bar{\psi}^\alpha(x) (D_0 \psi)^\alpha(x) \right] + \kappa \sum_{x,\alpha,i} \bar{\psi}^\alpha(x) (D_i \psi)^\alpha(x) \quad (8)$$

$$S_J = \kappa_j \sum_x [\psi^{2tr}(x) C \gamma_5 \tau_2 \psi^1(x) - \bar{\psi}^1(x) C \gamma_5 \tau_2 \bar{\psi}^{2tr}(x)], \quad (9)$$

with

$$(D_i \psi)^\alpha(x) = (\gamma_i - 1) U_i(x) \psi^\alpha(x + \hat{i}) - (\gamma_i + 1) U_i^\dagger(x - \hat{i}) \psi^\alpha(x - \hat{i}), \quad (10)$$

$$(D_0 \psi)^\alpha(x) = (\gamma_0 - 1) U_0(x) e^\mu \psi^\alpha(x + \hat{0}) - (\gamma_0 + 1) U_0^\dagger(x - \hat{0}) e^{-\mu} \psi^\alpha(x - \hat{0}). \quad (11)$$

We also define

$$\beta_s = \frac{\beta}{\gamma_g}; \quad \beta_t = \gamma_g \beta; \quad \kappa_t = \gamma_q \kappa_s = \gamma_q \kappa. \quad (12)$$

The parameters γ_g and γ_q are the bare gluon and quark anisotropies, which in our formalism will be taken to be independent.

Substituting these expressions into (5) (and dropping the $|_{a_s}$ from all partial derivatives as it will be understood), we then readily derive

$$\begin{aligned} \frac{\varepsilon_g}{T^4} &= -\xi \left(\frac{N_\tau a_\tau}{N_s a_s} \right)^3 \left\langle \frac{\partial S_G}{\partial \xi} \right\rangle \\ &= \frac{3N_\tau^4}{\xi^2 N_c} \left[\langle \text{Re Tr } U_{ij} \rangle \left(\gamma_g^{-1} \frac{\partial \beta}{\partial \xi} + \beta \frac{\partial \gamma_g^{-1}}{\partial \xi} \right) \right. \\ &\quad \left. + \langle \text{Re Tr } U_{i0} \rangle \left(\gamma_g \frac{\partial \beta}{\partial \xi} + \beta \frac{\partial \gamma_g}{\partial \xi} \right) \right]. \quad (13) \end{aligned}$$

This coincides with the first part of Eq. (17) of Ref. [13]. The terms in angled brackets are the average spatial and temporal plaquettes respectively, and the terms multiplying them are what are usually known as the Karsch coefficients. In the weak coupling isotropic limit $\beta \rightarrow \infty, \gamma_g = 1$ we have

$$\frac{\partial \gamma_g}{\partial \xi} = -\frac{\partial \gamma_g^{-1}}{\partial \xi} = 1; \quad \frac{\partial \beta}{\partial \xi} = -a \frac{\partial \beta}{\partial a} = 0, \quad (14)$$

and we recover the expression used in [7, 8]:

$$\frac{\varepsilon_g^0}{T^4} = \frac{3N_\tau^4 \beta}{N_c} [\langle \text{Re Tr } U_{i0} \rangle - \langle \text{Re Tr } U_{ij} \rangle]. \quad (15)$$

The quark contribution to the energy density is given by

$$\begin{aligned} \frac{\varepsilon_q}{T^4} &= -\xi \left(\frac{N_\tau a_\tau}{N_s a_s} \right)^3 \left\langle \frac{\partial S_Q}{\partial \xi} \right\rangle \\ &= -\frac{N_\tau^4}{\xi^2} \left[\left\langle \sum_i \bar{\psi} D_i \psi \right\rangle \frac{\partial \kappa}{\partial \xi} + \langle \bar{\psi} D_0 \psi \rangle \left(\gamma_q \frac{\partial \kappa}{\partial \xi} + \kappa \frac{\partial \gamma_q}{\partial \xi} \right) \right]. \quad (16) \end{aligned}$$

The terms in angled brackets are calculated using a stochastic estimator. Note a potentially useful identity

$$\gamma_q \kappa \langle \bar{\psi} D_0 \psi \rangle + \kappa \sum_i \langle \bar{\psi} D_i \psi \rangle + \langle \bar{\psi} \psi \rangle = -\text{Tr } 1 = -4N_c N_f. \quad (17)$$

Note that we have taken explicit account of the minus sign associated with closed fermion loops in the definition of the bilinear expectation values, ie. $\langle \bar{\psi} \Gamma \psi \rangle \equiv$

$-\text{Tr}(\Gamma M^{-1})$. It is therefore sufficient to evaluate the first and third terms on the LHS, enabling the second term, which enters into Eq. (16), to be estimated. In the isotropic limit $\gamma_q = \xi = 1$ this reduces to

$$\frac{\varepsilon_q}{T^4} = N_\tau^4 \left[(4N_f N_c + \langle \bar{\psi} \psi \rangle) \kappa^{-1} \frac{\partial \kappa}{\partial \xi} - \kappa \frac{\partial \gamma_q}{\partial \xi} \langle \bar{\psi} D_0 \psi \rangle \right]. \quad (18)$$

In the weak coupling isotropic limit $\partial \kappa / \partial \xi = 0$, $\partial \gamma_q / \partial \xi = 1$ and we recover

$$\frac{\varepsilon_q^0}{T^4} = -N_\tau^4 \kappa \langle \bar{\psi} D_0 \psi \rangle, \quad (19)$$

which coincides up to an overall sign with the expression in [7, 8], where the fermion's Grassmann nature was ignored.

Finally, the diquark contribution is given by

$$\begin{aligned} \frac{\varepsilon_J}{T^4} &= \frac{N_\tau^4}{\xi^2} \left(\frac{\partial(\kappa j)}{\partial \xi} \right) \langle -\bar{\psi}^1 C \gamma_5 \tau_2 \bar{\psi}^{2tr} + \psi^{2tr} C \gamma_5 \tau_2 \psi^1 \rangle \\ &= \frac{2N_\tau^4}{\xi^2} \left(\frac{\partial j}{\partial \xi} + \frac{j}{\kappa} \frac{\partial \kappa}{\partial \xi} \right) \langle qq \rangle \end{aligned} \quad (20)$$

in the notation of [7]. However, in the $U(1)_B$ -symmetric limit $j \rightarrow 0$ the second term inside the brackets vanishes, and since this limit is always found at $j = 0$ for any anisotropy ξ , the first term also vanishes here.

Similarly, the trace anomaly is given by

$$T_{\mu\mu} \equiv \varepsilon - 3p = \frac{T}{V} \left\langle a_s \frac{\partial S}{\partial a_s} \Big|_\xi \right\rangle. \quad (21)$$

With our anisotropic action the quark and gluon contributions are given by

$$\begin{aligned} (T_{\mu\mu})_g &= \frac{3}{\xi^2 N_c} \left[\langle \text{Re Tr } U_{ij} \rangle \left(\gamma_g^{-1} a \frac{\partial \beta}{\partial a} + \beta a \frac{\partial \gamma_g^{-1}}{\partial a} \right) \right. \\ &\quad \left. + \langle \text{Re Tr } U_{i0} \rangle \left(\gamma_g a \frac{\partial \beta}{\partial a} + \beta a \frac{\partial \gamma_g}{\partial a} \right) \right], \end{aligned} \quad (22)$$

$$\begin{aligned} (T_{\mu\mu})_q &= \frac{1}{\xi^2} \left[\left\langle \sum_i \bar{\psi} D_i \psi \right\rangle a \frac{\partial \kappa}{\partial a} \right. \\ &\quad \left. + \langle \bar{\psi} D_0 \psi \rangle \left(\gamma_q a \frac{\partial \kappa}{\partial a} + \kappa a \frac{\partial \gamma_q}{\partial a} \right) \right]. \end{aligned} \quad (23)$$

However, in the isotropic limit, the bare anisotropies are always 1, and hence the derivatives $\partial \gamma_{g,q} / \partial a$ vanish. We are then left with the standard expressions for the trace anomaly,

$$(T_{\mu\mu})_g = -a \frac{\partial \beta}{\partial a} \frac{3}{N_c} \langle \text{Re Tr } U_{ij} + \text{Re Tr } U_{i0} \rangle, \quad (24)$$

$$(T_{\mu\mu})_q = -a \frac{\partial \kappa}{\partial a} \kappa^{-1} (4N_f N_c + \langle \bar{\psi} \psi \rangle). \quad (25)$$

Eqs. (24,25) differ from the expressions used in [7, 8] by an overall factor β and an overall sign respectively; the resulting error is corrected in this paper.

So, in order to evaluate the full energy density (ignoring $j \neq 0$) from Eqs. (13,16) we need the following, which go into the definition of the ‘‘Karsch coefficients’’:

$$\frac{\partial \beta}{\partial \xi}; \quad \frac{\partial \gamma_g}{\partial \xi}; \quad \frac{\partial \kappa}{\partial \xi}; \quad \frac{\partial \gamma_q}{\partial \xi}. \quad (26)$$

These are computed using the method presented in [13, 14]. In addition to the bare anisotropies we define the physical anisotropies $\xi_g = a_s / a_\tau$ as determined from gluonic observables such as the ‘‘sideways potential’’ [15], and $\xi_q = a_s / a_\tau$ as determined from a meson dispersion relation. For a parameter set corresponding to a *physical* system ξ_g and ξ_q should be equal, since otherwise a massless meson would not propagate at the correct speed of light; choosing the bare parameters to bring this about is a non-trivial tuning problem [13, 16]. In attempting to calculate the Karsch coefficients for the parameter set $\beta = 1.9$, $\kappa = 0.168$, we do not attempt this tuning, but rather simulate unphysical ensembles with either γ_g or γ_q set to unity; the parameters are given in Table III. In addition we use the isotropic ensembles given in Table I.

For each ensemble we compute the ratio $M = (m_\pi / m_\rho)^2$, the lattice spacing $a \equiv a_s$, the gluon anisotropy ξ_g (from the sideways potential) and the quark anisotropy ξ_q (from the pion dispersion relation). The quark and gluon anisotropies are combined to form the average anisotropy $\xi_+ = \frac{1}{2}(\xi_g + \xi_q)$ and the anisotropy mismatch $\xi_- = \xi_g - \xi_q$. Each of these quantities is fitted to a linear function in the bare parameters,

$$\xi_+ - 1 = a_1 \Delta \gamma_g + b_1 \Delta \gamma_q + c_1 \Delta \beta + d_1 \Delta \kappa, \quad (27)$$

$$\frac{a - a_0}{a_0} = a_2 \Delta \gamma_g + b_2 \Delta \gamma_q + c_2 \Delta \beta + d_2 \Delta \kappa, \quad (28)$$

$$\frac{M - M_0}{M_0} = a_3 \Delta \gamma_g + b_3 \Delta \gamma_q + c_3 \Delta \beta + d_3 \Delta \kappa, \quad (29)$$

$$\xi_- = a_4 \Delta \gamma_g + b_4 \Delta \gamma_q + c_4 \Delta \beta + d_4 \Delta \kappa, \quad (30)$$

where a_0 and M_0 are the values of a and M at the reference point $\beta = 1.9$, $\kappa = 0.168$, $\gamma_g = \gamma_q = 1$, and Δx is the deviation of the bare parameter x from its value at the same reference point. Inverting the 4×4 matrix of coefficients (a_i, b_i, c_i, d_i) gives us the ‘‘generalised Karsch coefficients’’, which are the derivatives of the bare parameters with respect to the ‘‘physical’’ parameters [32] ξ_+, ξ_-, a, M . The first column gives us the Karsch coefficients (26), while the second column gives us the beta functions $\partial \beta / \partial a, \partial \kappa / \partial a$.

Since we do not need to renormalise the pressure, knowledge of the beta-functions is not required here. However, we can use information about them to perform consistency checks. In the isotropic limit, two of the Karsch coefficients can be expressed in terms of beta-functions, since

$$\frac{\partial \beta}{\partial \xi} \Big|_{\xi=1} = -a \frac{\partial \beta}{\partial a}; \quad \frac{\partial \kappa}{\partial \xi} \Big|_{\xi=1} = -a \frac{\partial \kappa}{\partial a}. \quad (31)$$

We can also independently estimate the beta-functions from the isotropic results in Sec. II, by taking derivatives wrt a along lines of constant physics.

β_s	β_t	κ_s	κ_t	γ_g	γ_q	ξ_g	ξ_q	m_π/m_ρ	$a_s(\text{fm})$
1.90	1.90	0.1680	0.1680	1.0	1.0	0.968^{+2}_{-2}	1.07^{+2}_{-3}	0.807^{+5}_{-5}	0.178^{+4}_{-6}
2.37	1.52	0.168	0.168	0.8	1.0	0.720^{+2}_{-2}	0.853^{+14}_{-10}	0.805^{+4}_{-5}	0.177^{+4}_{-3}
1.27	2.83	0.168	0.168	1.5	1.0	1.321^{+5}_{-5}	1.32^{+4}_{-3}	0.648^{+8}_{-12}	0.125^{+3}_{-6}
1.90	1.90	0.180	0.157	1.0	0.87	0.747^{+4}_{-4}	0.78^{+4}_{-3}	0.746^{+21}_{-13}	0.107^{+3}_{-6}
1.90	1.90	0.147	0.192	1.0	1.3	1.146^{+4}_{-4}	1.53^{+2}_{-2}	0.946^{+1}_{-1}	0.229^{+7}_{-13}
1.80	1.80	0.1740	0.1740	1.0	1.0	0.989^{+3}_{-3}	1.03^{+1}_{-3}	0.777^{+6}_{-8}	0.177^{+6}_{-8}
1.90	1.90	0.1685	0.1685	1.0	1.0	0.945^{+5}_{-6}	0.98^{+3}_{-3}	0.760^{+10}_{-18}	0.153^{+7}_{-18}
2.00	2.00	0.1620	0.1620	1.0	1.0	0.921^{+4}_{-5}	0.99^{+3}_{-4}	0.829^{+9}_{-9}	0.166^{+1}_{-3}
2.00	2.00	0.1630	0.1630	1.0	1.0	0.881^{+5}_{-5}	1.04^{+5}_{-4}	0.773^{+11}_{-11}	0.148^{+2}_{-1}

TABLE III: Anisotropic lattice parameters and anisotropy results. The uncertainties are purely statistical.

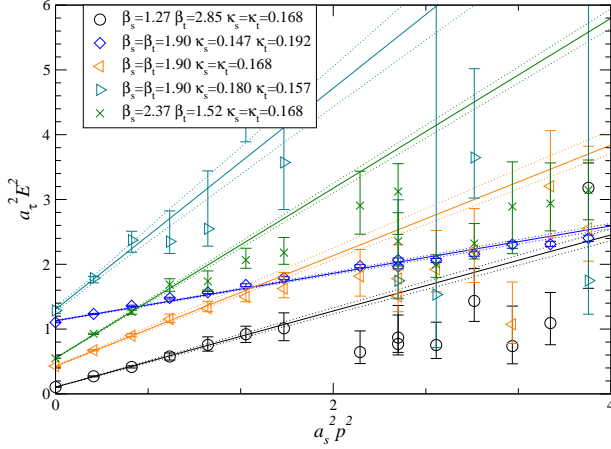


FIG. 2: The pion dispersion relation from the anisotropic $12^3 \times 24$ lattices in Table III.

Results for the observables on our anisotropic lattices as well as the isotropic lattices used in this study, are given in Table III. Figs 2 and 3 illustrate the determination of the quark and gluon anisotropies respectively. The gluon anisotropy in Fig. 3 was computed using [17]

$$\xi_g = \frac{V_{xt}(R_2) - V_{xt}(R_1)}{V_{xy}(R_2) - V_{xy}(R_1)}, \quad (32)$$

where $V_{xt}(x), V_{xy}(x)$ are the potentials obtained from Wilson loops in the (x, t) and (x, y) plane respectively,

$$W_{ss}(x, y) \sim Z_{xy} e^{-yV_{xy}(x)}, W_{st}(x, t) \sim Z_{xt} e^{-tV_{xt}(x)}, \quad (33)$$

which is valid for large x and t, y . The fermion anisotropy is determined from the pion dispersion relation,

$$a_\tau^2 E^2 = a_\tau^2 m_\pi^2 + \frac{a_s^2 p^2}{\xi_q^2}. \quad (34)$$

Hence, a straight-line fit of $a_\tau^2 E^2$ vs $a_s^2 p^2$, as shown in Fig. 2, will give the anisotropy ξ_q .

The results of the fits to (27)–(30) are shown in Table IV. We see that the χ^2 per degree of freedom is very

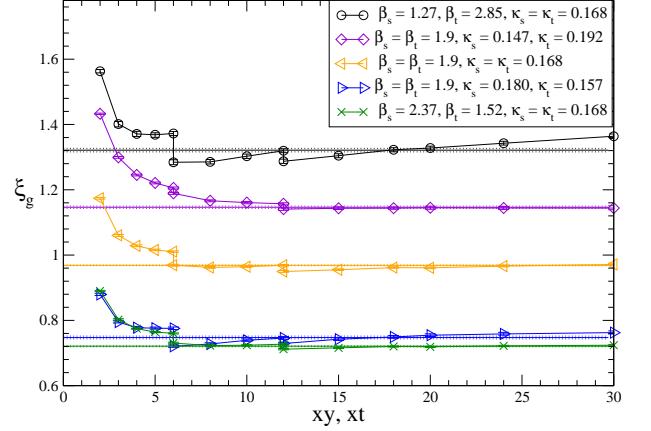


FIG. 3: The gauge anisotropy from the anisotropic $12^3 \times 24$ lattices in Table III, computed according to Eq. (32).

i	a_i	b_i	c_i	d_i	χ^2/N_{df}
ξ_+	$1 \quad 0.761^{+30}_{-29}$	$-1.66^{+0.70}_{-0.49}$	$-2.58^{+0.70}_{-0.39}$	-39^{+12}_{-7}	19.4
a	$2 \quad -0.503^{+48}_{-55}$	$-5.14^{+0.79}_{-1.42}$	$-5.94^{+0.74}_{-1.01}$	-88^{+10}_{-17}	2.8
M	$3 \quad -0.531^{+29}_{-46}$	$0.15^{+1.10}_{-0.57}$	-0.59^{+96}_{-61}	-15^{+16}_{-8}	22.6
ξ_-	$4 \quad 0.096^{+28}_{-29}$	-0.84^{+52}_{-85}	-0.46^{+38}_{-73}	-6^{+12}_{-12}	1.9

TABLE IV: Results for the fits to Eqs. (27)–(30). χ^2/N_{df} is the χ^2 per degree of freedom for each fit.

high, especially for the average anisotropy and the mass ratio fits. This indicates that our linear approximation breaks down in this region, something which in the case of the anisotropy may be seen directly from the numbers in Table III, where a nonlinear response of the physical anisotropies (and, indeed the lattice spacing) to the bare anisotropies is evident. To account for this, we would need to either include nonlinear terms in our *Ansatz* or employ smaller anisotropies (which would again require much higher statistics to determine the coefficients with sufficient precision). That is beyond the scope of this study.

The generalised Karsch coefficients are presented in Table V. We see that although the anisotropy deriva-

c_i	$\frac{\partial c_i}{\partial \xi_+}$	$a \frac{\partial c_i}{\partial a}$	$M \frac{\partial c_i}{\partial M}$	$\frac{\partial c_i}{\partial \xi_-}$
γ_g	0.90 $^{+4}_{-14}$	-0.51 $^{+19}_{-10}$	0.13 $^{+32}_{-58}$	1.4 $^{+1.2}_{-1.6}$
γ_q	0.13 $^{+40}_{-5}$	0.22 $^{+12}_{-70}$	-0.55 $^{+2.11}_{-0.29}$	-2.9 $^{+5.7}_{-0.6}$
β	0.59 $^{+0.24}_{-1.37}$	-1.4 $^{+2.3}_{-0.5}$	3.7 $^{+1.9}_{-7.0}$	8 $^{+8}_{-19}$
κ	-0.052 $^{+69}_{-15}$	0.075 $^{+24}_{-99}$	-0.22 $^{+35}_{-8}$	-0.39 $^{+88}_{-23}$

TABLE V: Results for the generalised Karsch coefficients $\partial c_i/\partial x_i$. The numbers in the first column are the actual Karsch coefficients, while the second column gives the beta functions.

c_i	$a \frac{\partial c_i}{\partial a}$	$M \frac{\partial c_i}{\partial M}$
β	-1.02 $^{+17}_{-29}$	0.73 $^{+26}_{-13}$
κ	0.057 $^{+15}_{-9}$	-0.047 $^{+8}_{-16}$

TABLE VI: Results for the beta functions $a\partial c_i/\partial a$ and mass derivatives $M\partial c_i/\partial M$, computed from fits to the isotropic data sets.

tives are reasonably well determined, other quantities, including the beta functions, have quite large uncertainties. The same has been found previously in real QCD with anisotropic lattices [14]. It is likely that the extraction of the lattice spacing from the static quark potential is the main limiting factor here, and that a high-precision lattice spacing determination from for example the Wilson flow [18] (which may also be used to determine the gauge anisotropy [19]) would help in this respect.

A surprising result is the small value for the coefficient $\partial\gamma_q/\partial\xi$, which comes out between 0.1 and 0.2, in contrast to $\partial\gamma_g/\partial\xi$, which has a value close to 1 as expected. It is possible that this is related to the breakdown of the linear approximation, and that including non-linear terms might bring this coefficient closer to 1. As we shall see in Sec. IV C, this has a significant impact on the resulting energy density.

The coefficients $a\partial\gamma_{g,q}/\partial a$ should be zero in the isotropic limit. While consistent or nearly consistent with zero within errors, the central values in Table V are fairly large. If we could constrain these to be exactly zero, our overall uncertainties might be reduced. We also see that Eq. (31) is satisfied within the admittedly large uncertainties. Again, it might improve the accuracy of our determination if these equations could be constrained to hold exactly.

We may also use m_π/m_ρ instead of $M = (m_\pi/m_\rho)^2$ as our mass observables in the fits. We find that repeating the analysis above with this choice does not change the results for the Karsch coefficients and beta functions by much.

We have also computed the beta functions separately from a 2-dimensional fit to the isotropic ensembles only. The results are shown in Table VI. As we can see, the two approaches give consistent results, suggesting that the systematic uncertainties of the method are under

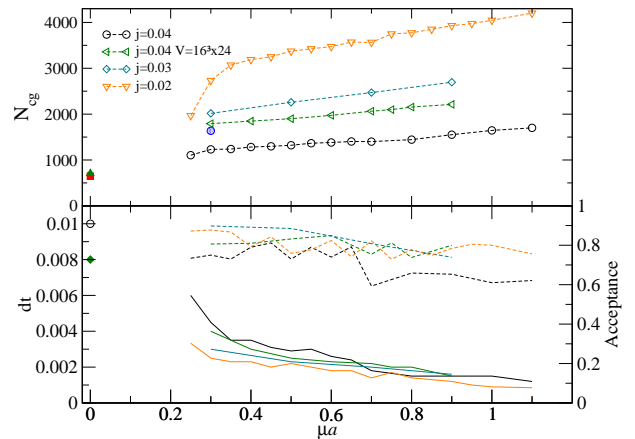


FIG. 4: The number of conjugate gradient iterations N_{cg} per inversion, step size dt (solid lines) and acceptance rates (dashed lines) for our simulations on $N_\tau = 24$ lattices.

reasonable control. The numbers are also roughly consistent with (but somewhat larger than) the crude estimates used in Ref. [8], where a simple backward derivative approximation was used.

IV. RESULTS AT $\mu \neq 0$

We now focus on the ($\beta = 1.9, \kappa = 0.1680$) parameter set, and explore the interior of the (T, μ) plane for these bare couplings. Results for $j = 0.04$ on the $12^3 \times 24$ lattices were already presented in [8]. Now, with the addition of data for $j = 0.02$ and, for some selected μ -values, $j = 0.03$, we can extrapolate all our results to the $j = 0$ limit. The details of this extrapolation will be discussed in Section IV A, as will our treatment of finite lattice spacing and finite volume lattice artefacts.

We have also explored higher temperatures with data at $N_\tau = 16, 12, 8$, and studied finite volume effects with the addition of a 16^3 spatial volume. The temperatures are $T = 47, 70, 94$ and 141 MeV for $N_\tau = 24, 16, 12$ and 8 respectively. Details of our data sets are given in Tables VII–X. Figure 4 shows the computational effort for the $N_\tau = 24$ lattices in terms of the number of conjugate gradient iterations per inversion and the molecular dynamics stepsize. It is evident from this figure that simulations in the dense region at the lowest j -value are 1–2 orders of magnitude more costly than those of the vacuum.

A. Diquark source extrapolation and lattice artefacts

In Fig. 5 we show the diquark condensate $\langle qq \rangle$ as a function of the diquark source j for $\mu a = 0.3, 0.5, 0.6, 0.9$ on the $12^3 \times 24$ lattice. We have attempted to fit the behaviour with three different functional forms: linear

$a\mu$	$aj = 0.02$	$aj = 0.03$	$aj = 0.04$	
			$N_s = 12$	$N_s = 16$
0.25	250		560	
0.30	514	315	632	500
0.325	250		560	
0.35	284		1248	
0.375	250		660	
0.38			552	
0.40	256		712	500
0.425	264		592	
0.45	368		768	
0.46			680	
0.47			468	
0.48			712	
0.49			716	
0.50	253	270	699	730
0.525			556	
0.55	260		168	
0.575			314	
0.60	256		172	510
0.65	260		644	
0.70	253	250	476	560
0.75	255		600	
0.80	257		616	600
0.85	255			
0.90	250	260	316	560
0.95	257			
1.00	250		600	
1.10	252		504	

TABLE VII: Number of trajectories for $\mu \neq 0$, $\beta = 1.9$, $\kappa = 0.168$, $N_\tau = 24$ ($T = 47$ MeV). The $ja = 0.02, 0.03$ configurations all have $N_s = 12$. All trajectories have average length 0.5.

$a\mu$	0.300	0.400	0.450	0.500	0.525	0.550	0.575
N_{traj}	500	560	2000	2520	2045	2000	2550
$a\mu$	0.600	0.625	0.650	0.675	0.700	0.800	0.900
N_{traj}	2520	2520	560	560	520	540	500

TABLE VIII: Chemical potential values and number of trajectories for the $12^3 \times 16$ lattices ($T = 70$ MeV). The diquark source is $ja = 0.04$ in all cases. All trajectories have average length 0.5.

$a\mu$	0.200	0.250	0.275	0.300	0.325	0.350	0.360	0.375	0.390
$N(0.04)$	1000	2500	2520	2520	2800	4900	2100	4900	1300
$a\mu$	0.400	0.425	0.450	0.500	0.600	0.700	0.800	0.900	
$N(0.04)$	1080	1050	1050	1164	1128	600	510	540	
$N(0.02)$	500			512	310	300	250	255	

TABLE IX: Chemical potential values and number of trajectories for the $16^3 \times 12$ lattices ($T = 94$ MeV). $N(0.04)$ and $N(0.02)$ are the number of trajectories for $ja = 0.04$ and 0.02 respectively. All trajectories have average length 0.5.

$a\mu$	0.100	0.200	0.300	0.400	0.500	0.600	0.700	0.800	0.900
$N(0.04)$	1000	1000	1000	1050	1050	1200	1000	1000	1000
$N(0.02)$				1000	1000	1000	1000		

TABLE X: As Table IX, for the $16^3 \times 8$ lattices ($T = 141$ MeV).

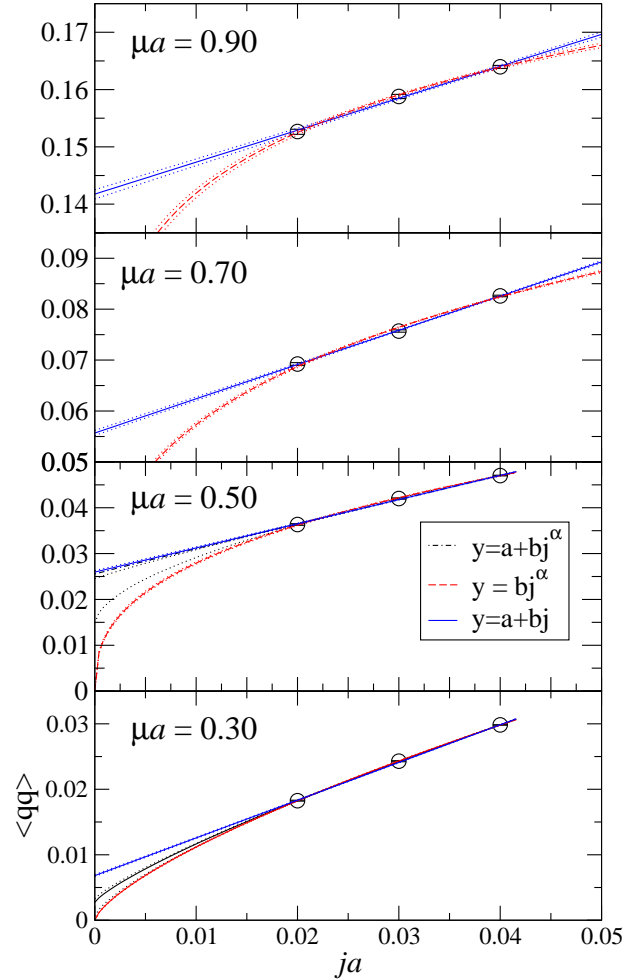


FIG. 5: The diquark condensate $\langle qq \rangle$ as a function of diquark source j , for the $12^3 \times 24$ lattice, together with extrapolations to $j = 0$. The dotted lines denote the 68% confidence interval for each fit. At $\mu = 0.50$ the central value lies outside the 68% confidence interval.

($\langle qq \rangle = A + Bj$), power-law ($\langle qq \rangle = Bj^\alpha$) and constant + power ($\langle qq \rangle = A + Bj^\alpha$). Our results are summarised in Table XI. We find that a linear fit works reasonably well except for $\mu a = 0.3$, where a pure power-law works well, confirming that the diquark condensate is indeed zero at this point. At $\mu a = 0.5$, neither functional form gives a very good fit, but the constant + power fit gives a result for the extrapolated diquark condensate consistent with the linear form. Note that the constant + power fit is always far less stable than the two others, but for $\mu a \geq 0.5$ the extrapolated values are consistent with those from

μa	0.3	0.5	0.7	0.9
Linear fit $A + Bj$				
A	0.0068(1)	0.0260(3)	0.0557(5)	0.1418(8)
χ^2	7.5	3.3	0.06	1.05
Power law fit Bj^α				
α	0.709(6)	0.376(7)	0.261(6)	0.104(5)
χ^2	0.23	2.1	15.1	1.03
Power + constant fit $A + Bj^\alpha$				
A	0.0027^{+5}_{-21}	0.025^{+1}_{-11}	0.058^{+2}_{-3}	0.129^{+6}_{-13}
α	0.36^{+2}_{-6}	0.50^{+1}_{-29}	$1.0^{+1.0}_{-0.4}$	0.21^{+7}_{-4}

TABLE XI: Parameters for $j \rightarrow 0$ extrapolations of the diquark condensate $\langle qq \rangle$. Note that the power + constant fit is a 3-parameter fit to 3 data points, and hence there is no χ^2 for this fit.

μa	0.3	0.5	0.7	0.9
Linear fit $A + Bj$				
A	0.0000(5)	0.0128(9)	0.0407(17)	0.190(3)
χ^2	6.8	3.7	0.04	0.04
Power law fit Bj^α				
α	0.95(17)	0.18(5)	0.20(3)	0.076(15)
χ^2	6.7	4.8	0.07	0.11
Power + constant fit $A + Bj^\alpha$				
A	0.000^{+5}_{-24}	0.0162^{+2}_{-2}	0.025^{+11}_{-46}	0.185^{+9}_{-64}
α	0.21^{+18}_{-19}	-0.0171^{+13}_{-0}	0.11^{+8}_{-1}	0.29^{+47}_{-13}

TABLE XII: Parameters for $j \rightarrow 0$ extrapolations of the quark number density n_q , for the $12^3 \times 24$ lattice.

the linear fit.

The results for other observables are similar. As an illustration of this, the corresponding fits for the quark number density n_q summarised in Table XII. Based on these findings, we use a linear function as our default extrapolation model for all observables, keeping in mind that this will distort the results somewhat in the régime $\mu a \lesssim 0.5$.

Next, we discuss our treatment of lattice artefacts in the context of the quark number density n_q . As in previous works, it will prove convenient to express results in terms of dimensionless ratios, eg. n_q/n_q^{SB} , where n_q^{SB} is the result for non-interacting quarks. However, even for free quarks artifacts due to non-zero lattice spacing and finite spatial volume are non-negligible, resulting in significant departures from the result in continuum and thermodynamic limits, and very careful discussion is required. Insight into both UV and IR artefacts can be gleaned by considering the ratio $n_{SB}^{\text{lat}}/n_{SB}^{\text{cont}}(T=0)$, calculated for two different volumes using the formula given in [7], and shown in Fig. 6. The correction is numerically large across extensive portions of the μ -axis. The oscillatory behaviour seen for $\mu a < 0.8$ is an IR artefact known

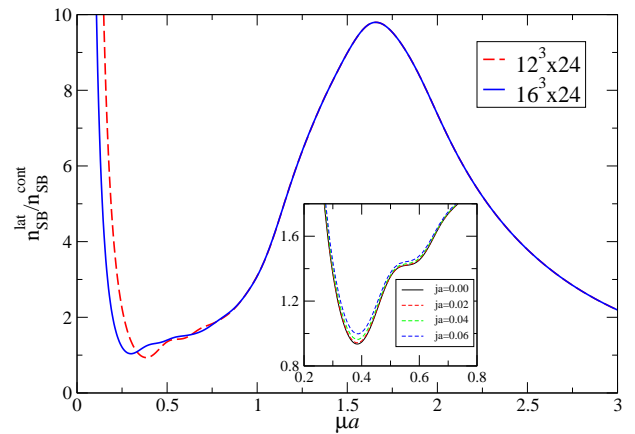


FIG. 6: Ratio $n_{SB}^{\text{lat}}/n_{SB}^{\text{cont}}$ evaluated for free massless quarks on both $12^3 \times 24$ and $16^3 \times 24$ lattices. The inset shows the same ratio for the $12^3 \times 24$ lattice, for four different values of the diquark source j .

to arise from the non-sphericity of the Fermi surface resulting from the discretisation of momentum space [20].

As an illustration of these effects, in Fig. 7 we show the normalised quark number density n_q/n_{SB} at fixed diquark source $ja = 0.04$, with two different choices for n_{SB} . In the upper panel we have normalised by n_{SB} for the corresponding lattice volumes, while in the lower panel we have used the same normalisation for all lattices. We have chosen to use n_{SB} for a $16^3 \times 24$ lattice for this normalisation; note that this choice is purely a matter of convenience, the purpose being to easily compare the raw numbers for n_q from different lattices. We see that there is no difference between our raw numbers for n_q on the $12^3 \times 24$ and $16^3 \times 24$ lattices at $j = 0.04$; however n_{SB} for the 12^3 lattice has a dip around $\mu a \simeq 0.4$, while on the 16^3 lattice this feature has moved to smaller μ . This dip coincides with the peak in n_q/n_{SB} seen in the upper panel of Fig. 7, giving rise to a spurious discrepancy in the normalised results for the two volumes.

By contrast, the correction factor coincides on the two volumes for $\mu a > \mathcal{O}(1)$, suggesting that the considerable departure from unity at large μ is due to UV effects. As we can see in the inset of Fig. 6, the diquark source has a negligible effect on the noninteracting quark density, and hence any significant j -dependence in our results must arise from interactions.

Based on these findings, we will in the following present our results for n_q and the pressure p , as well as the quark number susceptibility χ_q , using both the noninteracting lattice and continuum expressions to normalise our data. This will allow us to assess the magnitude of IR and UV lattice artefacts. For the energy density and trace anomaly, where gluonic contributions are significant, we will instead normalise by μ^4 .

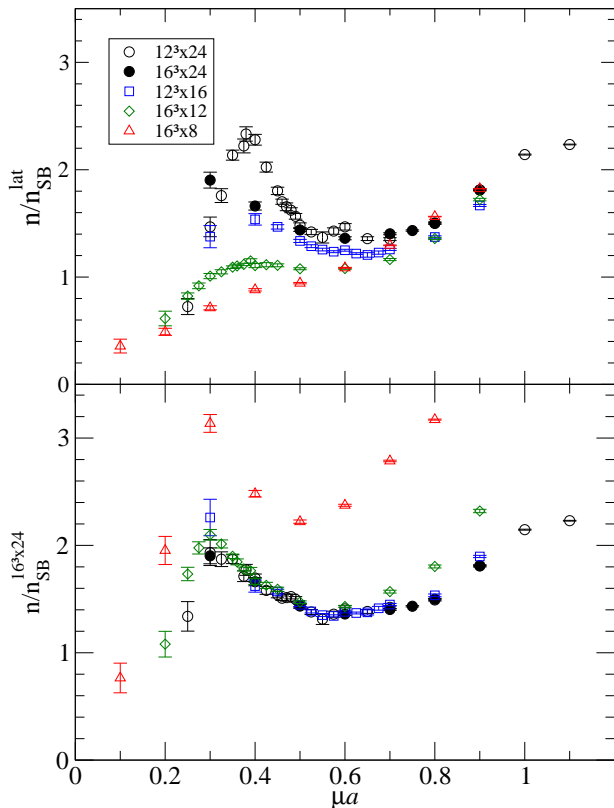


FIG. 7: The quark number density at $ja = 0.04$ for different lattice volumes, divided by the density for a noninteracting gas of lattice quarks on the same volume (top) and on a fixed volume of $16^3 \times 24$ (bottom).

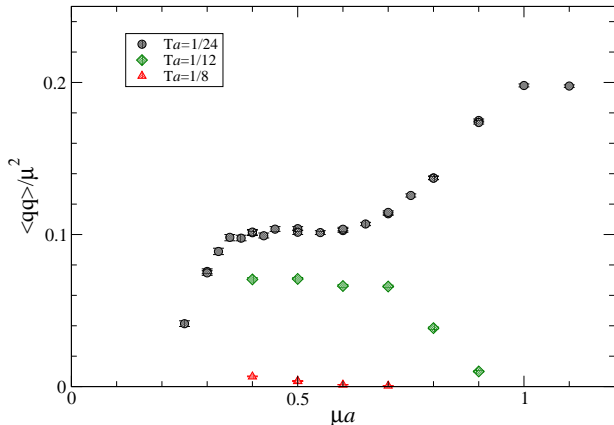


FIG. 8: The diquark condensate $\langle qq \rangle / \mu^2$ extrapolated to $j = 0$ for $N_\tau = 24, 12, 8$ ($T = 47, 94, 141$ MeV).

B. Order parameters and phase structure

Figure 8 shows the diquark condensate,

$$\langle qq \rangle = \langle \psi^{2tr} C \gamma_5 \tau_2 \psi^1 - \bar{\psi}^1 C \gamma_5 \tau_2 \bar{\psi}^{2tr} \rangle, \quad (35)$$

as a function of chemical potential, for the $N_\tau = 24, 12$ and 8 lattices. In the case of a weakly-coupled BCS con-

densate at the Fermi surface, the diquark condensate, which is the number density of Cooper pairs, should be proportional to the area of the Fermi surface, ie $\langle qq \rangle \sim \mu^2$. This is to be contrasted with chiral perturbation theory (χ PT) [21], which for $\mu \gg \mu_o$ at leading order predicts $\langle qq \rangle$ to be μ -independent.

For the lowest temperature $T = 47$ MeV ($N_\tau = 24$) we see an almost perfect proportionality in the region $0.35 \lesssim \mu a \lesssim 0.6$. The lower limit of this region roughly coincides with the onset chemical potential $\mu_o \approx m_\pi/2 \approx 0.33a^{-1}$, below which both the quark number density and diquark condensate is expected to be zero. The reason we see a gradual rise from $\mu a \approx 0.25$ is our use of a linear Ansatz for the $j \rightarrow 0$ extrapolation, which is not valid in this régime, as discussed in Section IV A. For $\mu a \gtrsim 0.6$, $\langle qq \rangle / \mu^2$ rises again before possibly reaching a new plateau at $\mu a \approx 1.0$. This is possible evidence of a transition to a new state of matter at high density, but at these large densities the impact of lattice artifacts cannot be excluded.

At $T = 70$ MeV ($N_\tau = 16$) we are not in a position to perform a $j \rightarrow 0$ extrapolation, but from the $ja = 0.04$ data we see only a mild suppression in $\langle qq \rangle$, and only for $\mu a \gtrsim 0.8$. Since the results are almost indistinguishable from those at $T = 47$ MeV we do not show them here.

At $T = 94$ MeV ($N_\tau = 12$) we see that $\langle qq \rangle$ is significantly smaller for all values of μ and drops dramatically above $\mu a \gtrsim 0.7$. This gives us the first indications of the transition between the diquark-condensed and the normal phase. At $T = 141$ MeV ($N_\tau = 8$) we find that the diquark condensate is zero at all μ , confirming that the system is in the normal phase at this temperature. A systematic investigation including more temperatures and an extrapolation to $j = 0$ at all temperatures will be required to establish the exact location and nature of this transition.

Finally, comparing the numbers from the $12^3 \times 24$ and $16^3 \times 24$ lattices, no evidence of any significant finite volume effects are found, except at $\mu a = 0.9$ where the condensate on the smaller volume is slightly suppressed.

Figure 9 shows the order parameter for deconfinement, the Polyakov loop $\langle L \rangle$, for our four different temperatures. It has been renormalised using (4), using the μ -independent renormalisation constant Z_L already computed in Sec. II. We see that for each temperature T , $\langle L \rangle$ increases rapidly from zero above a chemical potential $\mu_d(T)$ which we may identify with the chemical potential for deconfinement. However, since L is a convex function of μ at all T , it is not possible to use the variation of L with μ to define $\mu_d(T)$. In the absence of a more rigorous criterion, we have taken the point where L crosses the value it takes at $T_d(\mu = 0)$, $L_d = 0.6$, to define $\mu_d(T)$. The results are shown in Fig. 10, with error bars denoting the range $L_d = 0.5-0.7$. To more accurately locate the deconfinement line, we will need to perform a temperature scan for fixed μ -values, as was done for $\mu = 0$.

For our lowest temperature ($N_\tau = 24$), the renormalised Polyakov loop is too noisy for any quantitative

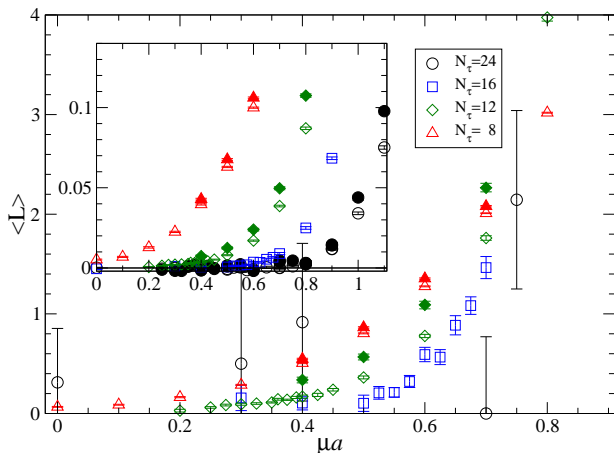


FIG. 9: The renormalised Polyakov loop as a function of chemical potential, for all temperatures. The open symbols are for $ja = 0.04$; the filled symbols are extrapolated to $j = 0$. The inset shows the unrenormalised Polyakov loop.

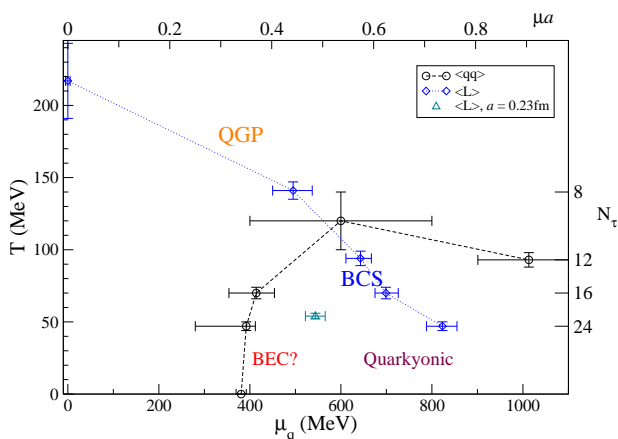


FIG. 10: A tentative phase diagram, including the location of the deconfinement transition in the (μ, T) plane, determined from the renormalised Polyakov loop, and the transition to the diquark condensed $\langle qq \rangle \neq 0$ phase. Also shown is the deconfinement point from Ref. [7].

conclusions to be drawn. This is because the signal (which is consistent with 0 for $\mu a < 0.75$) as well as the statistical noise are multiplied by the large renormalisation factor $Z_L^{24} = 2084$. However, the unrenormalised Polyakov loop L_0 , shown in the inset of Fig. 9, exhibits the same qualitative behaviour as for the higher temperatures. We also find that there are no significant volume effects, while the diquark source tends to suppress the Polyakov loop slightly. At $\mu a \approx 0.75$ we see that the curves for the renormalised Polyakov loop at the different temperatures cross, so that at higher μ , L is smaller for higher temperatures. This, however, depends on the renormalisation scheme: if we had instead imposed the condition that $L_R = 0.5$ at $N_\tau = 4, \mu = 0$, the curves would not cross.

The estimates of critical chemical potentials for both

deconfinement and superfluidity can be translated into a tentative phase diagram, shown in Fig. 10. It is worth reiterating that the points on the phase boundaries are rough estimates only, since we do not have a precise criterion for the transition. In Section IV D we will present results for a different measure of deconfinement, the quark number susceptibility. We also show the estimate from the coarser lattice in Ref. [7]. Clearly, a combination of temperature effects and lattice artefacts is responsible for the discrepancy between the μ_d -values quoted in [7, 8].

In Fig. 10 we also show our estimate of the transition between the superfluid and the normal phase. Again, since we do not yet have $j \rightarrow 0$ extrapolated data at all temperatures, and because our temperature grid is fairly coarse, these transition points are also only rough estimates.

In summary, from the order parameters we find signatures of three different regions (or phases): a normal (hadronic) phase with $\langle qq \rangle = 0, \langle L \rangle \approx 0$; a BCS (quarkyonic) region with $\langle qq \rangle \sim \mu^2$ at low T and intermediate to large μ ; and a deconfined, normal phase with $\langle qq \rangle = 0, \langle L \rangle \neq 0$ at large T and/or μ . We cannot exclude a deconfined superfluid phase with $\langle L \rangle > 0, \langle qq \rangle \neq 0$ at large μ and intermediate T .

After extrapolating our results to zero diquark source, we see no evidence of a BEC region described by χ PT, with $\langle qq \rangle \sim \sqrt{1 - \mu_o^4/\mu^4}$ [21], in contrast with earlier work with staggered lattice fermions [2]. This may be because we do not have a clear separation of scales between the Goldstone diquark scale and more massive states, and hence the region of tightly bound diquarks is very narrow. A more pessimistic scenario is that the BEC region is masked by the poor chiral properties of Wilson fermions. Simulations with lighter quarks may help clarify this.

C. Equation of state

We now turn to the bulk thermodynamics of the system: the quark number density n_q , the pressure p and the energy density ε . Figure 11 shows the quark number density n_q for $N_\tau = 24, 12$ and 8, extrapolated to zero diquark source. In the top panel we have normalised by the density n_{SB}^{lat} for noninteracting fermions on the same lattice volumes ($12^3 \times 24, 16^3 \times 12, 16^3$), as was done in [7, 8]. In the bottom panel, we have instead divided by the continuum, infinite-volume expression for noninteracting fermions at the same temperature and chemical potential. The difference between the two gives an indication of the lattice artefacts. We see that the density rises from zero at $\mu \approx \mu_o = 0.32a^{-1}$, and for the two lower temperatures is roughly constant and approximately equal to the noninteracting fermion density in the region $0.4 \lesssim \mu a \lesssim 0.7$. The peak at $\mu a \simeq 0.4$ in the $N_\tau = 24$ data in the upper panel is an artefact of the normalisation with n_{SB} for a finite lattice volume, as discussed in Sec. IV A; it would be absent if we instead

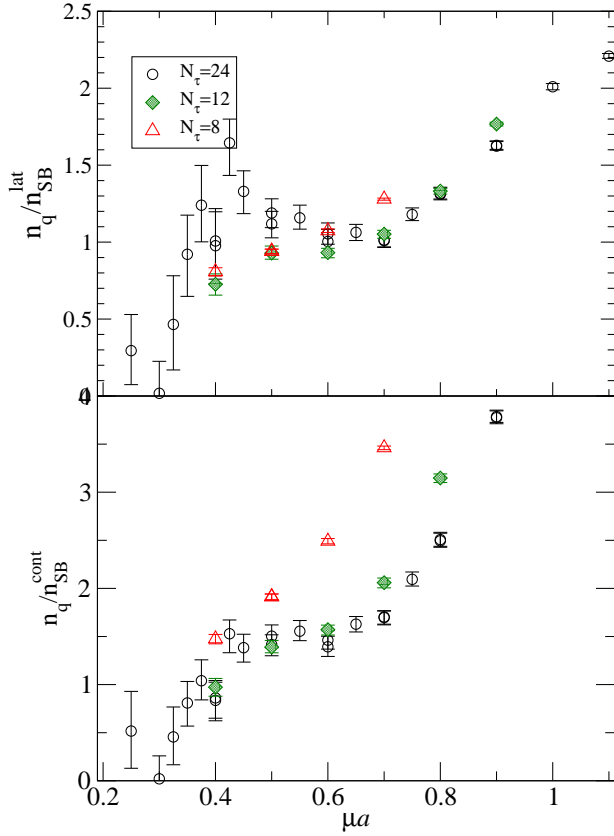


FIG. 11: The quark number density at $j = 0$, divided by the density for a noninteracting gas of lattice quarks (top) and continuum quarks (bottom).

normalised by n_{SB} for a 16^3 lattice, for which the raw data are identical within errors. We therefore conclude that our previous interpretation [7] of the peak in n_q/n_{SB} in this region as evidence of a BEC condensate described by χ PT was probably erroneous.

Our results for $N_\tau = 16$ are indistinguishable from the $N_\tau = 24$ results except for $\mu a \gtrsim 0.8$, where they also start increasing above the $N_\tau = 24$ values. The rise in n_q/n_{SB} for $\mu a \gtrsim 0.7$ may be a signal of a new phase, although in this region the influence of lattice artefacts cannot yet be ruled out.

We also note that n_q/n_{SB} for $N_\tau = 12$ rises above the corresponding $N_\tau = 24$ data for $\mu a \gtrsim 0.7$, where, according to the results of Sec. IV B, the hotter system is entering the deconfined, normal phase. The density for $N_\tau = 8$ does not show any plateau as a function of μ ; instead, n_q/n_{SB} shows a roughly linear increase in the region $0.4 \leq \mu a \leq 0.7$. This is suggestive of the system being in a different phase at this temperature.

These results lend further support to our previous conjecture that in the intermediate-density region the system is in a “quarkyonic” phase: a confined phase (all excitations are colourless) that can be described by quark degrees of freedom. We reiterate that because of the large explicit breaking of chiral symmetry in our simulations,

we cannot say anything at this point about chiral symmetry restoration, another characteristic of the quarkyonic phase conjectured in Ref. [9]. We will come back to this issue in Sec. IV E.

Next we discuss pressure, which as the negative of the free energy density, may be calculated via the integral of any thermodynamic observable along an appropriate contour. It is particularly convenient to integrate along the μ -axis via $p = \int_{\mu_0}^{\mu} n_q d\mu$, since the cutoff does not change. Here μ_0 is chosen so that $p(\mu_0) = 0$ to good approximation; in the limit $T \rightarrow 0$ μ_0 should coincide with the onset μ_o .

In our analysis the integral is readily approximated by a trapezoidal rule; as always, we present data normalised by the free field value p_{SB} , a procedure not uniquely defined away from the continuum limit. We have examined three schemes:

$$\left(\frac{p}{p_{SB}}\right)_0 = (p_{SB}^{\text{cont}}(\mu))^{-1} \int_{\mu_0}^{\mu} n_q(\mu') d\mu', \quad (36)$$

$$\left(\frac{p}{p_{SB}}\right)_I = (p_{SB}^{\text{lat}}(\mu))^{-1} \int_{\mu_0}^{\mu} n_q(\mu') d\mu', \quad (37)$$

$$\left(\frac{p}{p_{SB}}\right)_{II} = (p_{SB}^{\text{cont}}(\mu))^{-1} \int_{\mu_0}^{\mu} \frac{n_{SB}^{\text{cont}}}{n_{SB}^{\text{lat}}}(\mu') n_q(\mu') d\mu', \quad (38)$$

where

$$p_{SB}^{\text{cont}} = \frac{N_f N_c}{12\pi^2} \left(\mu^4 + 2\pi^2 \mu^2 T^2 + \frac{7\pi^4}{15} T^4 \right) \quad (39)$$

is the continuum pressure for a free gas of quarks, and p_{SB}^{lat} the corresponding value obtained by summing over free quark modes on the finite lattice. Versions (37) and (38) were both studied in [7], whereas only $(p/p_{SB})_{II}$ was used in [8, 22].

Fig. 12 shows the results for data taken with $ja = 0.04$, as well as the $j \rightarrow 0$ extrapolated data for $N_\tau = 24$. In scheme II lattice data are “corrected” for artefacts *before* integrating. The results clearly inherit the bump at $\mu a \simeq 0.45$ also manifest in Fig. 7, which we now believe to be an IR artefact. However, this bump is absent (or strongly suppressed) in the $j \rightarrow 0$ limit, mirroring the absence of a significant bump in the upper panel of Fig. 11. This extrapolation reduces the ratio p/p_{SB} from approximately 1.5 to approximately one in the quarkyonic regime. By contrast the scheme 0 data have the ratio p/p_{SB} substantially exceeding unity in the large- μ regime above deconfinement, which probably reflects the fact that UV artefacts are not being fully corrected here. For this reason we now prefer scheme I, where for the coldest lattice p/p_{SB} has a plateau with value ≈ 1 (after $j \rightarrow 0$) in the suspected quarkyonic region, only rising to ≈ 2 at large μ . Again, therefore, we conclude that for low T there is a range of μ where thermodynamic quantities scale approximately the same as free quarks; that the evidence for a peak above onset matching the expectations of χ PT has substantially diminished; and

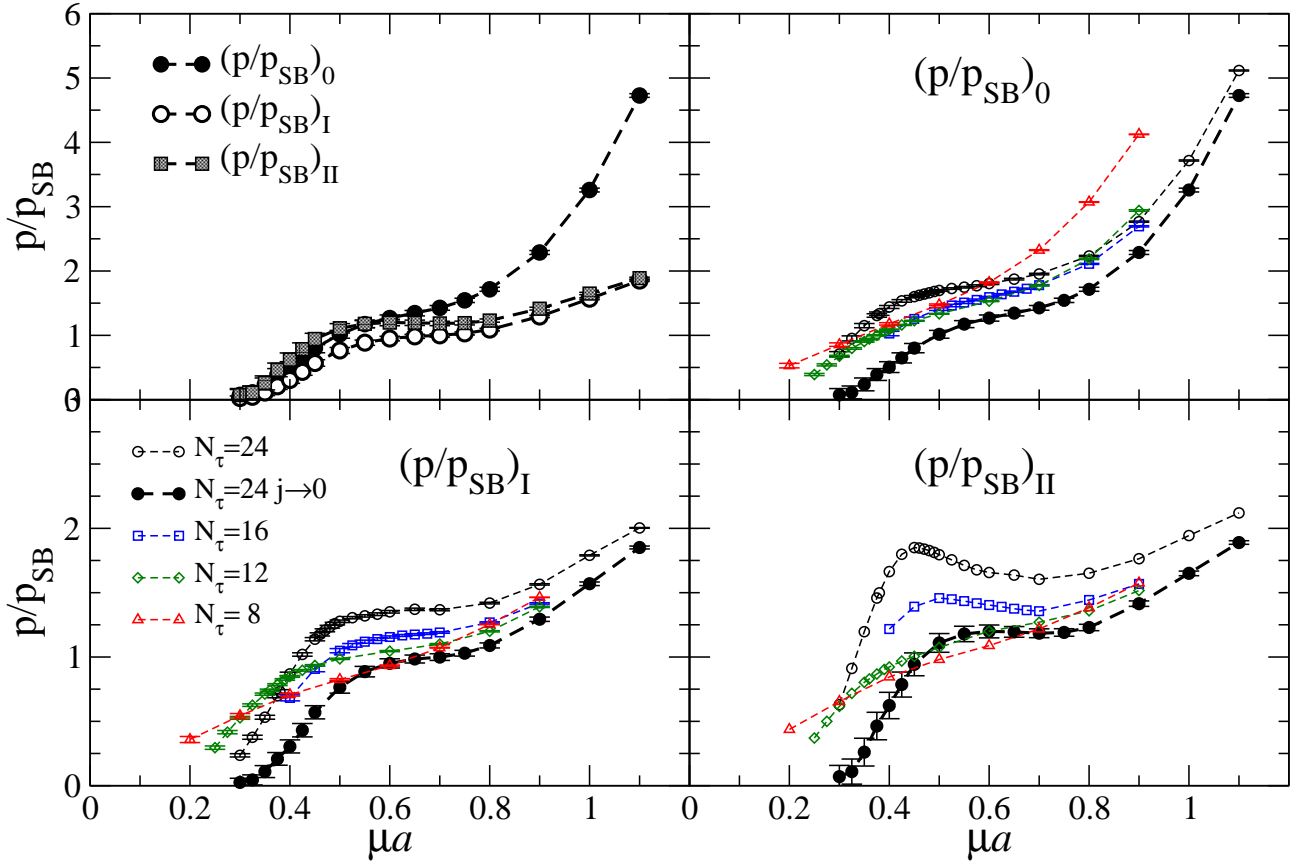


FIG. 12: p/p_{SB} vs. μa for $ja = 0.04$ and various temperatures. Also shown are values extrapolated to $j = 0$ for $N_\tau = 24$. Top left: $(p/p_{SB})_{0,I,II}$ for $j \rightarrow 0$, $N_\tau = 24$. Top right: $(p/p_{SB})_0$. Bottom left: $(p/p_{SB})_I$. Bottom right: $(p/p_{SB})_{II}$.

that p/p_{SB} rises above unity in the deconfined regime. By $T = 141$ MeV ($N_\tau = 8$), however, the ratio rises monotonically and the distinction between these different regimes is largely washed out. It is clear, however, that the full story will only emerge once the continuum and thermodynamic limits are both taken with care.

The quark and gluon contributions to the energy density, for $ja = 0.04$, are shown in the upper panel of Fig. 13. We see that the quark energy density is almost independent of temperature for all temperatures, while the gluon energy density shows a clearly different behaviour only for the highest temperature. We find that the gluon energy density is independent of the diquark source within errors, so these results are representative for the $j \rightarrow 0$ extrapolated data. The quark contribution is sensitive to the diquark source in the low- μ region, as can be seen from the $j \rightarrow 0$ extrapolated data also shown in Fig. 13.

Comparing these results with the unrenormalised (and unextrapolated) results in Figs 1 and 3 of Ref. [8], we see a dramatic difference. Clearly, the proper renormalisation is crucial to any reliable determination of the energy density, and in particular it is clear that the terms proportional to $\partial\beta/\partial\xi$ and $\partial\kappa/\partial\xi$ in (13) and (16) respectively cannot be ignored. To illustrate this more clearly,

we show in Fig. 14 the quark contribution to the energy density on the $12^3 \times 24$ lattice at $ja = 0.04$, computed using different values for the Karsch coefficients. The open circles correspond to the unrenormalised energy density which was presented in Ref. [8] (note that the normalisation is different). The other data sets correspond to different values of $\partial\gamma_q/\partial\xi$, with $\partial\kappa/\partial\xi$ set to the value of -0.052 that was determined in Sec. III. We have chosen to use the tree-level value of 1, the value 0.131 determined in Sec. III, and a value of 0.8, which is similar to the value found for $\partial\gamma_g/\partial\xi$, and at the margins of our 95% confidence interval. We see that using the correct (non-zero) value for $\partial\kappa/\partial\xi$ is most important at low μ , where this alone changes the sign of ε_q . At large μ , the $\partial\gamma_q/\partial\xi$ term will dominate, as it does at tree level.

It should be noted that the uncertainties in the Karsch coefficients are not included in the total uncertainties in the plots shown here. On the basis of Fig. 14 one may conclude that these uncertainties will have an effect of $\mathcal{O}(100\%)$ in the energy density.

Although ε_q appears to be negative at least for low μ , and possibly for all μ -values considered here, the total energy density $\varepsilon = \varepsilon_g + \varepsilon_q$, shown in the bottom panel of Fig. 13, remains positive or consistent with zero everywhere in the $j \rightarrow 0$ limit. Although on the face of it a

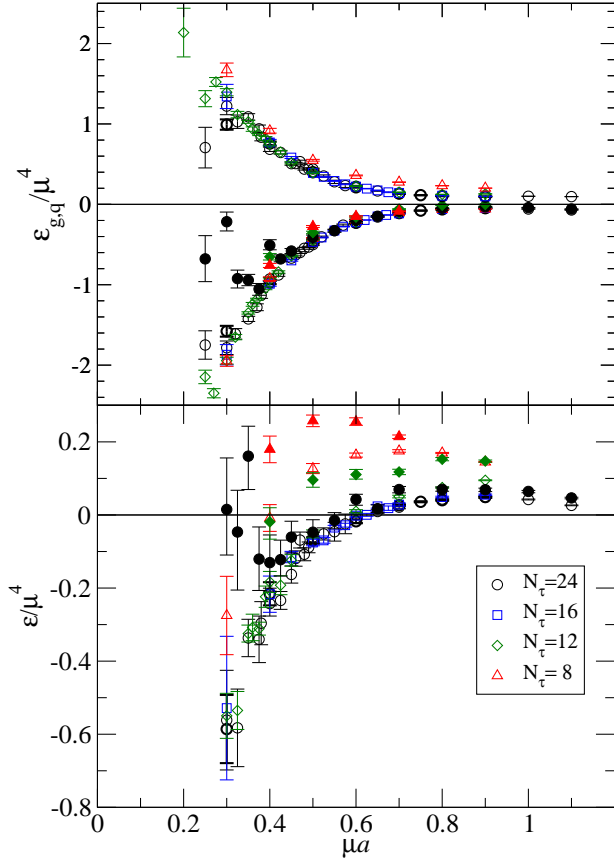


FIG. 13: Top: Renormalised quark (negative numbers) and gluon (positive numbers) energy density divided by μ^4 , at various temperatures, for $ja = 0.04$ (open symbols) and extrapolated to $j = 0$ (filled symbols). Bottom: total energy density divided by μ^4 .

negative value for ε_q is surprising, it is notable that the renormalised quark energy density shown in Fig. 13 has a qualitative resemblance to the unrenormalised energy density (16) measured for QC₂D with $N_f = 4$ Wilson quark flavors in Fig. 5 of Ref. [22]. The parameters used in that study correspond to a much finer lattice, with $a/\sqrt{\sigma}$ having a value approximately one-third that used here. It is conceivable, therefore, that the Karsch coefficients for $N_f = 4$ fall far closer to their free-field values, and hence their neglect in [22] is much better justified, reinforcing the conclusion that $\varepsilon_q(\mu) < 0$.

Finally, we consider the trace anomaly, computed according to Eqs (24), (25), which is shown in Fig. 15. With the correct expression (25), we now find the quark contribution to be negative for all μ , whereas in [7, 8] it had erroneously been presented as positive. Since the beta-functions only enter into the expressions as overall constants, and our updated values are not dramatically different from those used in Ref. [8], the qualitative behaviour of the $N_\tau = 24, ja = 0.04$ data is the same as previously reported in Ref. [8], apart from the sign of the quark contribution.

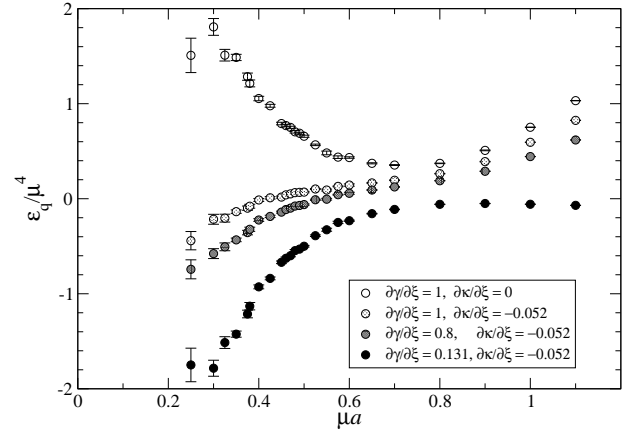


FIG. 14: Renormalised quark energy density divided by μ^4 density at $T = 47$ MeV ($N_\tau = 24$), $ja = 0.04$, for different values of the Karsch coefficients $\partial\gamma_q/\partial\xi, \partial\kappa/\partial\xi$.

For small and intermediate μ , the gluon and quark contributions have opposite signs and similar magnitudes, leading to a nearly vanishing total trace anomaly in the region $0 \leq \mu a \lesssim 0.7$. The gluon contribution decreases for $\mu \gtrsim 0.5$ and becomes negative for $\mu a \gtrsim 0.75$, while the quark contribution has a plateau for $0.5 \lesssim \mu a \lesssim 0.75$ and increases rapidly in magnitude thereafter. This leads to a negative total trace anomaly at large μ , which corresponds to the positive and increasing pressure $p = (\varepsilon - T_{\mu\mu})/3$ observed in Fig. 12.

We see no difference in the trace anomaly between the two lowest temperatures, $T = 47$ and 70 MeV. At $T = 94$ MeV and 141 MeV ($N_\tau = 12$ and 8) the gluon contribution becomes larger (or less negative) and the quark contribution becomes more negative at large μ . The net effect of this, however, is to leave the total trace anomaly nearly unchanged.

We find that the trace anomaly depends only weakly on the diquark source for nearly all T and μ . The main effect is to increase the gluon contribution at large μ and T , and to decrease the magnitude of the quark contribution at low T , for large and small μ . It is quite striking that there appears to be little or no dependence on either temperature or diquark source in the region $\mu_o \lesssim \mu \lesssim 0.55/a$.

Once again, it is instructive to compare with the $N_f = 4$ study of Ref. [22]. In that case (see figs. 6 and 8 of [22]), after taking into account the incorrect sign for the quark contribution, the gluon unrenormalised contribution to $T_{\mu\mu}$ is negative for all $\mu \lesssim \mu_d$, while the quark contribution is positive, which is the opposite of what we observe here. However, this still leaves open the possibility of the two contributions nearly cancelling, giving rise to nearly-conformal matter in the quarkyonic region.

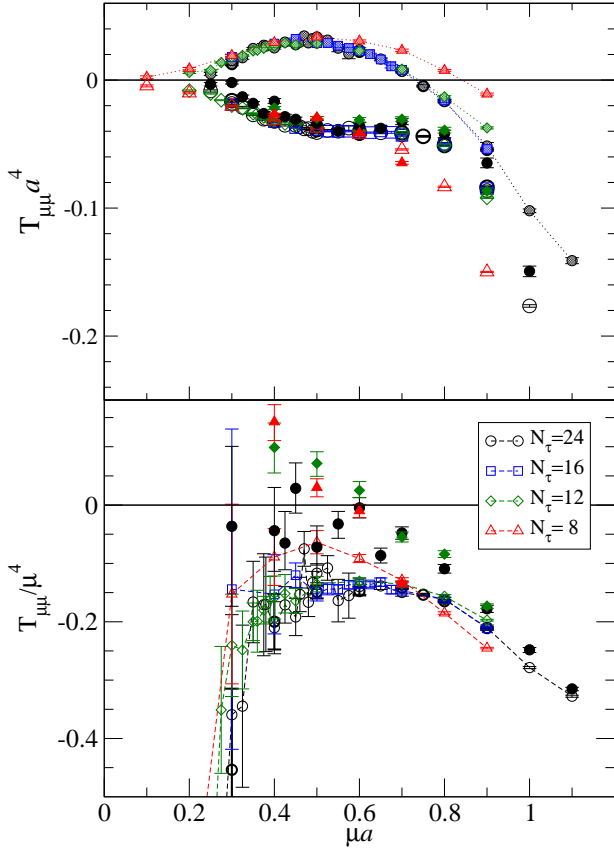


FIG. 15: Top: gluon (shaded symbols, dotted lines) and quark (open symbols) contributions to the trace anomaly, at $ja = 0.04$. The filled symbols denote the quark contributions extrapolated to $j = 0$. Bottom: Total trace anomaly divided by μ^4 , for $ja = 0.04$ (open symbols, dashed lines) and extrapolated to $j = 0$ (filled symbols).

D. Quark number susceptibility

In a mathematical sense the Polyakov loop is a well-defined signal for deconfinement, at least in pure gauge theories; physically it reveals something about the behaviour of static color sources, which are well approxi-

mated by heavy quarks, in a baryonic medium. Recent studies of a non-relativistic formulation of QC_2D [23] took the first step beyond the static approximation, and revealed a non-trivial T - and μ -dependence for s -wave states formed from heavy quarks. Another observable related to confinement is the quark number susceptibility $\chi_q \equiv \partial n_q / \partial \mu$. This observable is usually thought of as encoding the fluctuations in the baryon (or quark) number, and is of particular interest as a measure of confinement or deconfinement of light quark degrees of freedom [24–27]. If quarks are confined inside hadrons, the fluctuations of the quark number and hence the susceptibility will be suppressed, since increasing the quark number entails exciting a baryon, which requires a large amount of energy. If quarks are not confined, it is possible to excite a single quark, which requires much less energy, giving a larger quark number susceptibility.

This link between χ_q and deconfinement is clear in the case of QCD, where all baryons are heavy. In the case of QC_2D the situation is less clear, since the lightest baryons are the pseudo-Goldstone diquarks, and large fluctuations are possible even in the confined phase. Nonetheless, it is of great interest to study fluctuations in quark number at large density and low temperature. The only previous such study is Ref. [28], where the Dyson–Schwinger equation in the rainbow approximation was employed. Hence QC_2D offers an opportunity for a first systematic non-perturbative study of χ_q in this régime.

For an ideal gas of massless (continuum) quarks and gluons, at temperature T and chemical potential μ , we have:

$$n_{SB}^{\text{cont}} = N_f N_c \left(\frac{\mu T^2}{3} + \frac{\mu^3}{3\pi^2} \right), \quad (40)$$

$$\chi_{SB}^{\text{cont}} = N_f N_c \left(\frac{T^2}{3} + \frac{\mu^2}{\pi^2} \right). \quad (41)$$

Now consider the quark action (1) rewritten in the form $\bar{\Psi} \mathcal{M} \Psi$, where we have introduced the bispinors $\Psi \equiv (\psi_1, C^{-1} \tau_2 \bar{\psi}_2^{tr})^{tr}$, $\bar{\Psi} \equiv (\bar{\psi}_1, -\psi_2^{tr} C \tau_2)$; see Ref. [10] for details. From the definition of χ_q we have:

$$\chi_q = \frac{\partial n_q}{\partial \mu} = \frac{T}{V_s} \left\{ - \left\langle \left[-\bar{\Psi} \frac{\partial \mathcal{M}}{\partial \mu} \Psi \right] \right\rangle^2 + \left\langle \left[-\bar{\Psi} \frac{\partial \mathcal{M}}{\partial \mu} \Psi \right]^2 \right\rangle + \left\langle \left[-\bar{\Psi} \frac{\partial^2 \mathcal{M}}{\partial \mu^2} \Psi \right] \right\rangle \right\}. \quad (42)$$

From this equation we can identify four different terms:

$$T_1 = -\left\langle \left[-\bar{\Psi} \frac{\partial \mathcal{M}}{\partial \mu} \Psi \right]^2 \right\rangle = -\left\langle \text{Tr} \left[\mathcal{M}^{-1} \frac{\partial \mathcal{M}}{\partial \mu} \right] \right\rangle^2, \quad (43)$$

$$T_2 = +\left\langle \left[-\bar{\Psi} \frac{\partial \mathcal{M}}{\partial \mu} \Psi \right]^2 \right\rangle_{disc} = \left\langle \text{Tr} \left[\mathcal{M}^{-1} \frac{\partial \mathcal{M}}{\partial \mu} \right] \cdot \text{Tr} \left[\mathcal{M}^{-1} \frac{\partial \mathcal{M}}{\partial \mu} \right] \right\rangle, \quad (44)$$

$$C_1 = +\left\langle \left[-\bar{\Psi} \frac{\partial \mathcal{M}}{\partial \mu} \Psi \right]^2 \right\rangle_{conn} = -\left\langle \text{Tr} \left[\mathcal{M}^{-1} \frac{\partial \mathcal{M}}{\partial \mu} \mathcal{M}^{-1} \frac{\partial \mathcal{M}}{\partial \mu} \right] \right\rangle, \quad (45)$$

$$T_3 = +\left\langle \left[-\bar{\Psi} \frac{\partial^2 \mathcal{M}}{\partial \mu^2} \Psi \right] \right\rangle = \left\langle \text{Tr} \left[\mathcal{M}^{-1} \frac{\partial^2 \mathcal{M}}{\partial \mu^2} \right] \right\rangle. \quad (46)$$

The second term of Eq. (42) yields two terms, T_2 and C_1 , because there are two ways to contract the spinors.

The calculation of the traces is done using unbiased estimators, introducing N_η complex noise vectors η with the properties: $\langle \eta_x \rangle = 0$ and $\langle \eta_x \eta_y \rangle = \delta_{xy}$. For example, the determination of the trace, used for T_1 and T_2 , is based on the following relation:

$$\text{Tr} \left[\mathcal{M}^{-1} \frac{\partial \mathcal{M}}{\partial \mu} \right] = \frac{1}{N_\eta} \sum \eta_{x\alpha i}^* \left(\frac{\partial \mathcal{M}}{\partial \mu} \right)_{x\alpha i; y\beta j} \mathcal{M}_{y\beta j; z\gamma k}^{-1} \eta_{z\gamma k}. \quad (47)$$

Because two independent source vectors are required to compute T_2 , we refer to this term as ‘‘disconnected’’; the other three ‘‘connected’’ terms need only one source vector.

It turns out that the connected term gives an important contribution to χ_q at low and high values of the chemical potential and therefore cannot be considered negligible. Moreover, it changes sign around $\mu a \approx 0.66$. On the other hand, the terms T_1 and T_2 are equal within errors but with opposite sign, *i.e.*, their net contribution is consistent with zero everywhere, except possibly around the onset transition.

All the systematic issues discussed in Sec. IV A, regarding the normalisation of data with the same quantity calculated for free quarks, are also relevant for χ_q . In Fig. 16 we plot the ratio $\chi_q/\chi_{SB}^{\text{cont}}$, for four different temperatures, versus the chemical potential. For an ideal gas of quarks and gluons this ratio would be a constant, see Eq. (41), and we see that an approximate plateau is actually present for $a\mu \lesssim 0.55$, at least for the three lowest temperatures; after this value we can see a sharp increase of χ_q . The value of the plateau is $\chi_q/\chi_{SB} \approx 1.6$ which is higher than the ideal value of 1.0. Moreover, it is evident from this plot that χ_q is T -independent at low temperature, since there is no significant deviation in the behaviour of the three curves. This is to be contrasted with the Polyakov loop in Fig. 9, which shows deconfinement for three different values of $\mu = \mu_d(T)$, as the temperature is varied. Only for the highest temperature do we see a different behaviour signalling a different phase.

It is also instructive to compare the numerical results with the equations corresponding to Eq. (41) but taking

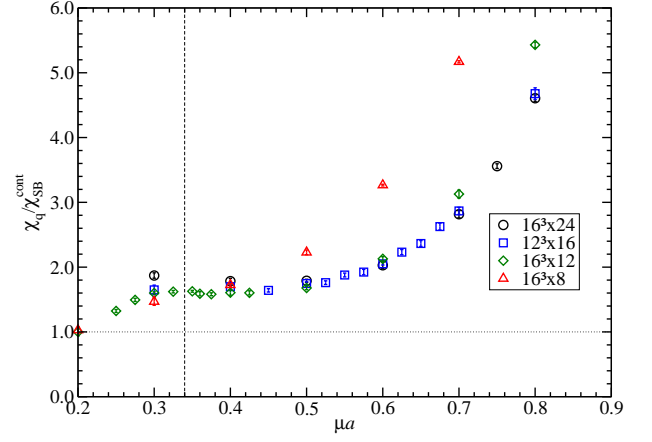


FIG. 16: Ratio $\chi_q/\chi_{SB}^{\text{cont}}$ versus μ , for $ja = 0.04$. The vertical dashed line marks the position of μ_o .

in account the finite volume and the lattice discretisation. In Eq.(26) of Ref. [7], the expression for the quark number density n_{SB}^{lat} for free Wilson fermions on the lattice is presented, from which χ_{SB}^{lat} is easily obtained. Fig. 17 plots the ratio $\chi_q/\chi_{SB}^{\text{lat}}$ for two values of the quark mass used in the determination of χ_{SB}^{lat} , the subtracted bare quark mass $m_q = 1/2\kappa - 1/2\kappa_c$ and the ‘constituent’ quark mass $m_c = m_\rho/2$. In this case we observe a different behaviour for $a\mu \lesssim 0.45$, but now in the quarkyonic regime there is a discernable plateau with a ratio compatible with one, *i.e.* the system is behaving as free fermions, with again an increase for higher values of μ . Fig. 17 demonstrates that the value of the mass used for the free fermions has a quantitative effect for this observable, in that the value of the plateau is shifted when the mass is increased, but this does not change the qualitative considerations. The results using m_q are almost identical those obtained setting $m = 0$. These plots again confirm the above scenario: we do not see any abrupt change for χ_q as a function of T , whereas the Polyakov loop becomes different from zero at a T -dependent μ_d . Again, something different seems to emerge for the highest temperature, $T = 141$ MeV ($N_\tau = 8$).

The effect of the diquark source is illustrated in Fig. 18,

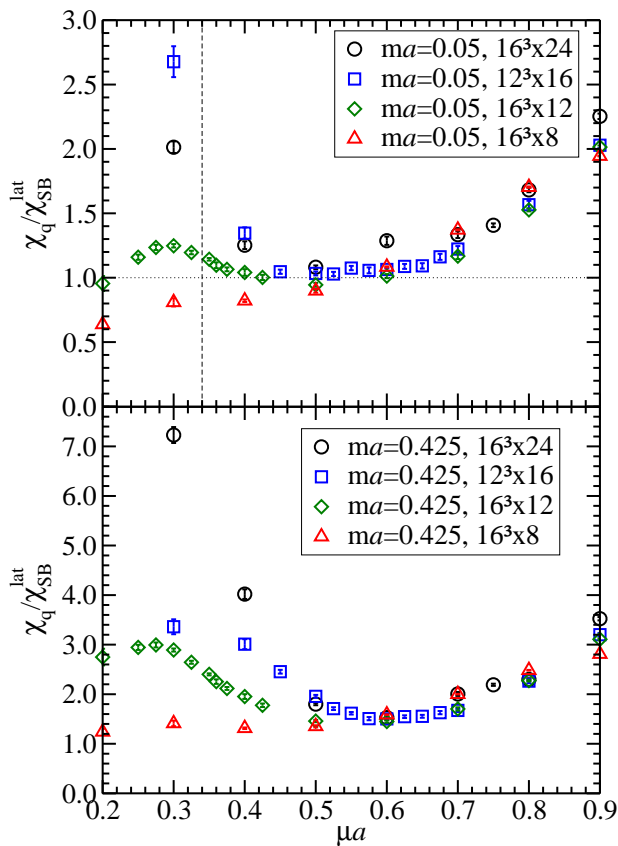


FIG. 17: The ratio between the measured quark number susceptibility at $ja = 0.04$ and the ideal value for *lattice* free fermions for two values of the fermion mass: $m_q = 0.05$ (top) and $m_c = 0.42$ (bottom). The vertical dashed lines mark the position of μ_o .

where we show $\chi_q/\chi_{SB}^{\text{lat}}(m_c)$ for the $12^3 \times 24$ lattice and $ja = 0.04, 0.02$ and 0 . We find that the diquark source only has a significant effect for low μ , where it increases the value of χ_q slightly.

E. A first look at chiral symmetry in the dense phase

An important issue which we have been hitherto unable to address is the chiral properties of the ground state once $\mu \geq \mu_o$. This issue is of course of general theoretical interest when the phase diagram of any non-abelian gauge theory is discussed; in the current context it is of particular interest since the original description of the quarkyonic phase in $SU(N_c)$ gauge theory was in terms of a chirally symmetric but confined medium, ie. one in which the chiral condensate $\langle \bar{\psi}\psi \rangle \rightarrow 0$ as the bare quark mass $m \rightarrow 0$ [9]. Later this picture was modified; chiral symmetry breaking via a translationally non-invariant “chiral spiral” was postulated in [29]. For theories of the class exemplified by QC_2D where the relevant mass scale is set by m_π , chiral symmetry is necessarily always bro-

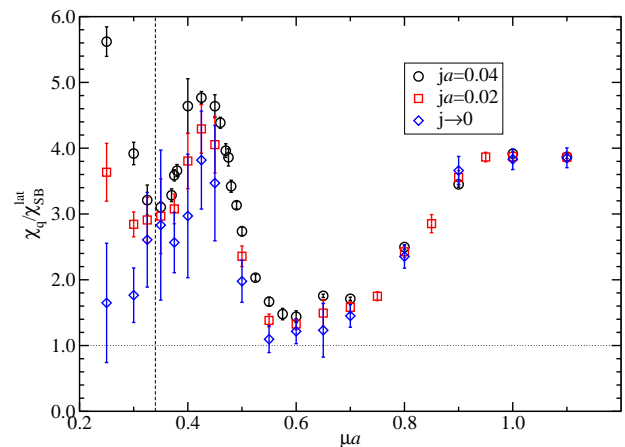


FIG. 18: The ratio between the measured quark number susceptibility at different diquark sources j and the ideal value for *lattice* free fermions with a fermion mass of $m_c = 0.42$. The vertical dashed lines mark the position of μ_o .

ken explicitly by a bare quark mass m ; in this case the question is how the condensate $\langle qq \rangle$ scales with $m \rightarrow 0$.

It is clearly desirable to determine the fate of chiral symmetry breaking for the case of QC_2D by a lattice calculation. Indeed, $\langle \bar{\psi}\psi \rangle$ was examined in early studies such as [2] using staggered lattice fermions, and reasonable quantitative agreement found over a decade of quark mass with the prediction of leading order χ PT for $T \rightarrow 0$, namely that for $\mu < \mu_o$ the chiral condensate is μ -independent, and for $\mu \geq \mu_o$

$$\langle \bar{\psi}\psi \rangle \propto \frac{m}{\mu^2}. \quad (48)$$

Unfortunately, since the global symmetries of staggered fermions do not coincide with those of continuum QC_2D [2], these results are not directly applicable. In any case, no attempt was made to explore beyond the régime of applicability of χ PT.

However, our use of Wilson fermions precludes any direct study in the current simulation, since this formulation violates chiral symmetry explicitly. Our strategy therefore is to calculate a chiral order parameter using a fermion formulation with manifest chiral and baryon number symmetries using the gauge backgrounds ensembles generated with Wilson quarks. The disparity between valence and sea quarks violates unitarity; we mitigate this uncontrolled approximation by tuning the mass of the valence quarks so that the pion mass coincides with that used in the simulation; once $\mu \neq 0$ the onset transition of the valence quarks should then at least coincide with the true value.

Rather than the obvious choice of staggered fermions for the valence quarks, we found it expedient to use the existing code for $N_f = 2$ Wilson fermions with the parameter r (which has the conventional value of unity in (2)) set to zero. For $j = 0$ this is equivalent to eight identical staggered fermions with mass

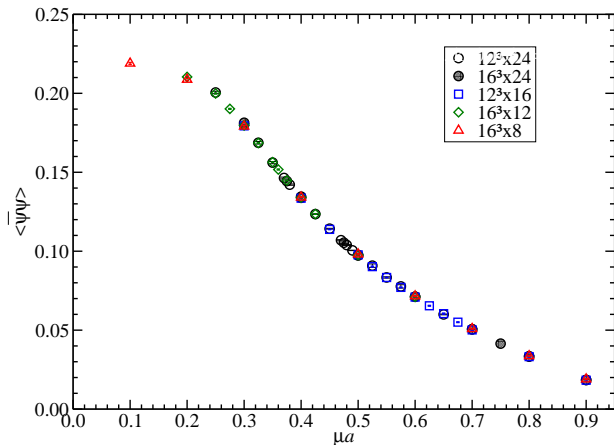


FIG. 19: $\langle \bar{\psi}\psi \rangle$ versus μ for $r = 0$, $ja = 0.04$ and $\kappa = 8.0$.

$m = (2\kappa)^{-1}$. For non-zero lattice spacing and $\mu \neq 0$ the action has a $U(8) \otimes U(8)$ global symmetry which is broken by $m \neq 0$ (explicitly) or $\langle \bar{\psi}\psi \rangle \neq 0$ (spontaneously) to $U(8)_V$ (the subscript denotes vectorlike), which incorporates the $U(1)_B$ of baryon number. A diquark source $j \neq 0$ breaks $U(8)_V$ to a $SU(2) \otimes SU(2)$ which preserves isospin but no longer includes $U(1)_B$.

By studying effective mass plots as the valence κ_V was varied we found that $\kappa_V = 8.0$ gave the closest match to the value $m_{\pi a} = 0.66(2)$ found for $\beta = 1.9$, $\kappa = 0.168$. Fig. 19 then shows the resulting chiral condensate as a function of μ for the various lattices studied. Note that $ja = 0.04$ throughout, since this was found to yield a less noisy and more stable signal – hence these results are not reproducible using pure staggered fermions. Two things are apparent; first the shape of the curve is in qualitative agreement with the old staggered results of [2] over the whole range of μ studied, and thus consistent with (48) assuming an onset $\mu_o a \simeq 0.3$. Secondly, the results are independent of temperature even up to $T = 141\text{MeV}$ ($N_\tau = 8$). It is also apparent that volume effects are negligible.

It appears that the chiral symmetry properties of the dense phase are well-described by χ PT. In a sense the issue of “chiral symmetry restoration” in QC_2D is academic, since the onset scale is set on the assumption that chiral symmetry is explicitly broken. Nonetheless, we can characterise the dense phase by whether $\lim_{m_V \rightarrow 0} \langle \bar{\psi}\psi(m_V) \rangle$ vanishes or not. We determine this by using three different values $\kappa_V = 8, 16$ and 40 , and observing that with the field normalisations implicit in (2),

$$\frac{\kappa_1^2 \langle \bar{\psi}\psi \rangle_1}{\kappa_2^2 \langle \bar{\psi}\psi \rangle_2} = \frac{m_2 \langle \bar{q}q \rangle_1}{m_1 \langle \bar{q}q \rangle_2} \begin{cases} = 1 & \langle \bar{\psi}\psi \rangle_0 = 0; \\ < 1 & \langle \bar{\psi}\psi \rangle_0 \neq 0, m_2 < m_1. \end{cases} \quad (49)$$

Here $\bar{q}q$ denotes the scalar quark bilinear with conventional normalisation and $\langle \bar{\psi}\psi \rangle_0$ is the chiral condensate

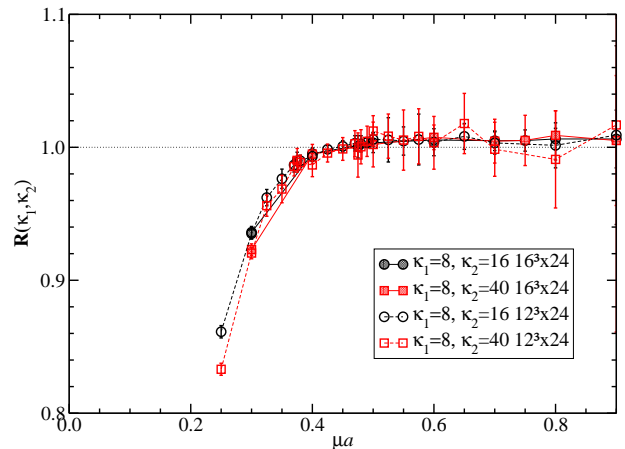


FIG. 20: The ratio $R(\kappa_1, \kappa_2) = [\kappa_1^2 \langle \bar{\psi}\psi \rangle_1] / [\kappa_2^2 \langle \bar{\psi}\psi \rangle_2]$ versus μ for $\kappa_0 = 8.0$ and $\kappa_1 = 16.0, 40.0$, on the $12^3 \times 24$ and $16^3 \times 24$ lattices with $ja = 0.04$.

in the massless limit. Fig. 20 shows this ratio plotted for both (8,16) and (8,40) valence mass pairs on the $12^3 \times 24$ and $16^3 \times 24$ lattices as a function of μ , and clearly indicates symmetry restoration for $\mu \gtrsim \mu_o$. Very similar plots are found for the other temperatures explored. We therefore conclude that the gauge field backgrounds at high baryon density in QC_2D are consistent with chiral symmetry being unbroken by a scalar condensate, although the exotic translationally-non-invariant scenario of [29] is not ruled out.

We find no significant difference between our results for the 12^3 and 16^3 lattices. This suggests that the chiral order parameter responds smoothly as m increases, with no indication at this stage of a phase transition (indeed the results are compatible with the predictions of chiral perturbation theory). However, in the absence of any systematic finite volume scaling study, and in light of the uncontrolled systematic uncertainties involved in our use of different actions and quark masses for sea and valence quarks, this should, like all the other results in this section, be taken as merely indicative.

V. CONCLUSIONS AND OUTLOOK

We have carried out the first extensive exploration of the phase diagram of two-color QCD (QC_2D) in the (T, μ) plane using first-principles lattice simulations. Our main findings are summarised in the tentative phase diagram of Fig. 10. We find evidence of three distinct regions:

1. A vacuum/hadronic phase, with $\langle qq \rangle = 0, \langle L \rangle \approx 0, \langle \bar{\psi}\psi \rangle \neq 0, n_q \approx 0$, at low T and $\mu \lesssim \mu_0 = m_\pi/2$;
2. A quarkyonic phase at low T and intermediate to large μ , which is confined ($\langle L \rangle \approx 0$) and characterised by a chiral condensate which vanishes in

the chiral limit, Stefan–Boltzmann scaling of bulk thermodynamic quantities (including a nearly vanishing trace anomaly) and BCS scaling of the di-quark condensate;

3. A deconfined quark–gluon plasma phase at high T (and/or large μ).

The main difference from our previous studies is that the BEC region has disappeared as a consequence of the $j \rightarrow 0$ extrapolation and a better understanding of the volume dependence and appropriate normalisation of our results. The BEC window would be expected to reappear for smaller m_π/m_ρ .

While we have clearly defined the finite-temperature deconfinement transition at $\mu = 0$, and find clear evidence of a deconfinement temperature that decreases as μ increases, the exact nature and location of this transition at large μ remain elusive. In order to pin down this transition, and also to precisely locate the superfluid-to-normal transition, we need to perform fine temperature scans by varying N_τ at fixed chemical potential. This is currently underway. We are also studying the static quark potential, which should give further insight into the nature of this transition.

For the first time in this paper we have attempted to calculate renormalised energy densities via an estimate of Karsch coefficients obtained from simulations on anisotropic lattices. We find the resulting corrections to our earlier results are substantial, and indeed strongly suggest the quark contribution $\varepsilon_q(\mu)$ is negative, implying that the physical requirement $\varepsilon_q + \varepsilon_g > 0$ arises from a cancellation between terms of opposite sign. Considerably greater accuracy will be required, therefore, before we can contemplate *eg.* using lattice results as input for the solution of the Tolman–Oppenheimer–Volkoff equations used in modelling relativistic stars.

We find that the quark number susceptibility χ_q is remarkably independent of the temperature up to $T \simeq 100\text{MeV}$, and stays close to its noninteracting value in the quarkyonic region. Most strikingly, it shows little if any sensitivity to the deconfinement transition, which occurs at different chemical potentials for our 4 temperature values.

The observation that χ_q is not a proxy for the Polyakov loop L in the régime of high quark number density suggests the following conjecture. In the quarkyonic region $\mu_o < \mu < \mu_d$ the bulk observables p , n_q , χ_q are approximately equal to the free-field values p_{SB} , n_{SB} and χ_{SB} . This is indicative of weakly self-bound quark matter, *ie.* with $E_F = \mu \approx k_F$. The transition at $\mu = \mu_d$ (which coincides with deconfinement as signalled by $L \neq 0$ only in the limit $T \rightarrow 0$) is to a more strongly self-bound régime with $E_F < k_F$. Since the quarkyonic phase is confining, we interpret weak self-binding as the quarks interacting via *binary* short-ranged interactions. For $\mu > \mu_d$, the interaction is screened and may not be much longer-ranged, but in this case deconfined quarks may interact with several other quarks in the vicinity leading to stronger

binding. These considerations are related to interactions within bulk quark matter, involving quarks with all energies less than the Fermi energy, which hence are not sensitive to temperature T .

By contrast, the observed temperature-sensitivity of the Polyakov loop L (see Fig. 9) suggests that in this case the relevant physics is associated with degrees of freedom close to the Fermi surface, which are readily thermally excited. These, of course, are the same degrees of freedom relevant for transport. Our results contrast with the findings of analytic and numerical studies of QCD-like theories at weak coupling in small volumes of characteristic scale $R \ll \Lambda_{QCD}^{-1}$ [27, 30], and a recent study of cold dense QCD with heavy quarks [31], both of which show a coincidence in the rise of L and χ_q . This suggests that a full description of deconfinement at high baryon density requires a thermodynamic limit and light, mobile degrees of freedom.

The main shortcoming of this study is that it has been performed with a single, relatively coarse lattice spacing. Although, as observed in Ref. [8], the main results are in qualitative agreement with the earlier results [7] obtained on a coarser lattice with $a = 0.23\text{fm}$, we also observe significant quantitative discrepancies, and substantial lattice artefacts for $\mu a \gtrsim 0.75$. To get this under control it will be necessary to repeat our simulations on a finer lattice. Thanks to the extensive investigation of parameter space reported in Sec. II, we are in a good position to carry this out, and these simulation are underway.

The large quark mass is another source of systematic uncertainty; moreover our discussion of chiral symmetry in Sec. IV E is at best exploratory, and must in due course be supplemented by a calculation respecting unitarity. It is clear that QC₂D must be treated as a separate theory and cannot be viewed as an approximation to QCD – indeed, the differences between the two theories become most stark in the chiral limit – and there is hence no need to attempt to match quark masses to those in the real world. Still, many analytical results have been obtained in or near the chiral limit. Also, as already mentioned, we would expect a BEC region to open up near μ_o for smaller values of m_π/m_ρ , and a fuller understanding of the BEC–BCS crossover would be valuable. For all these reasons, simulations with smaller quark masses would be of great interest, and such simulations are underway.

In addition to the quantities considered here, we are in the process of computing the Landau-gauge gluon and quark propagators. This will allow us to check the assumptions involved in model solutions of the superfluid or superconducting gap equation, and may form a direct link with functional methods such as the functional renormalisation group and Dyson–Schwinger equations. These do not suffer from the sign problem, but rely on assumptions regarding the form of propagators and higher order vertices. This will be addressed in a forthcoming publication.

Acknowledgments

This work is carried out as part of the UKQCD collaboration and the DiRAC Facility jointly funded by STFC, the Large Facilities Capital Fund of BIS and Swansea University. We thank the DEISA Consortium (www.deisa.eu), funded through the EU FP7 project RI-222919, for support within the DEISA Extreme Computing Initiative. The simulation code was adapted with

the help of Edinburgh Parallel Computing Centre funded by a Software Development Grant from EPSRC. JIS and SC acknowledge the support of Science Foundation Ireland grants 08-RFP-PHY1462, 11-RFP.1-PHY3193 and 11-RFP.1-PHY3193-STTF-1. JIS acknowledges the support and hospitality of the Institute for Nuclear Theory at the University of Washington, where part of this work was carried out. We warmly thank Joyce Myers and Seyong Kim for their help.

-
- [1] K. Fukushima and T. Hatsuda, Rept.Prog.Phys. **74**, 014001 (2011), [1005.4814].
- [2] S. Hands *et al.*, Eur. Phys. J. **C17**, 285 (2000), [hep-lat/0006018].
- [3] A. Maas, L. von Smekal, B. Wellegehausen and A. Wipf, Phys.Rev. **D86**, 111901 (2012), [1203.5653].
- [4] J. B. Kogut, D. K. Sinclair, S. J. Hands and S. E. Morrison, Phys. Rev. **D64**, 094505 (2001), [hep-lat/0105026].
- [5] S. Hands, P. Sitch and J.-I. Skullerud, Phys.Lett. **B662**, 405 (2008), [0710.1966].
- [6] T. Brauner, K. Fukushima and Y. Hidaka, Phys. Rev. **D80**, 074035 (2009), [0907.4905].
- [7] S. Hands, S. Kim and J.-I. Skullerud, Eur. Phys. J. **C48**, 193 (2006), [hep-lat/0604004].
- [8] S. Hands, S. Kim and J.-I. Skullerud, Phys. Rev. **D81**, 091502 (2010), [1001.1682].
- [9] L. McLerran and R. D. Pisarski, Nucl. Phys. **A796**, 83 (2007), [0706.2191].
- [10] P. Giudice, S. Hands and J.-I. Skullerud, PoS **LATTICE2011**, 193 (2011), [1110.6112].
- [11] S. Borsányi *et al.*, Phys.Lett. **B713**, 342 (2012), [1204.4089].
- [12] I. Montvay and G. Münster, *Quantum fields on a lattice* (Cambridge University Press, Cambridge, UK, 1994), Cambridge monographs on mathematical physics.
- [13] L. Levkova, T. Manke and R. Mawhinney, Phys.Rev. **D73**, 074504 (2006), [hep-lat/0603031].
- [14] R. Morrin, *A non-perturbative study of the renormalisation of action parameters in anisotropic lattice QCD with applications to finite temperature QCD*, PhD thesis, Trinity College Dublin, 2009.
- [15] T. R. Klassen, Nucl. Phys. **B533**, 557 (1998), [hep-lat/9803010].
- [16] R. Morrin, A. Ó Cais, M. Peardon, S. M. Ryan and J.-I. Skullerud, Phys. Rev. **D74**, 014505 (2006), [hep-lat/0604021].
- [17] M. Loan, T. Byrnes and C. Hamer, Eur.Phys.J. **C31**, 397 (2003), [hep-lat/0303011].
- [18] S. Borsányi *et al.*, JHEP **1209**, 010 (2012), [1203.4469].
- [19] S. Borsányi *et al.*, 1205.0781.
- [20] S. Hands and D. N. Walters, Phys. Lett. **B548**, 196 (2002), [hep-lat/0209140].
- [21] J. Kogut, M. Stephanov, D. Toublan, J. Verbaarschot and A. Zhitnitsky, Nucl. Phys. **B582**, 477 (2000), [hep-ph/0001171].
- [22] S. Hands, P. Kenny, S. Kim and J.-I. Skullerud, Eur.Phys.J. **A47**, 60 (2011), [1101.4961].
- [23] S. Hands, S. Kim and J.-I. Skullerud, Phys.Lett. **B711**, 199 (2012), [1202.4353].
- [24] Y. Aoki, Z. Fodor, S. Katz and K. Szabo, Phys.Lett. **B643**, 46 (2006), [hep-lat/0609068].
- [25] Wuppertal-Budapest Collaboration, S. Borsányi *et al.*, JHEP **1009**, 073 (2010), [1005.3508].
- [26] A. Bazavov *et al.*, Phys.Rev. **D80**, 014504 (2009), [0903.4379].
- [27] S. Hands, T. J. Hollowood and J. C. Myers, JHEP **1012**, 057 (2010), [1010.0790].
- [28] D.-K. He, Y. Jiang, H.-T. Feng, W.-M. Sun and H.-S. Zong, Chin.Phys.Lett. **25**, 440 (2008).
- [29] T. Kojo, Y. Hidaka, L. McLerran and R. D. Pisarski, Nucl. Phys. **A843**, 37 (2010), [0912.3800].
- [30] S. Hands, T. J. Hollowood and J. C. Myers, JHEP **1007**, 086 (2010), [1003.5813].
- [31] M. Fromm, J. Langelage, S. Lottini, M. Neuman and O. Philipsen, 1207.3005.
- [32] Strictly speaking, ξ_- is not a physical parameter since it denotes the deviation from the physical condition $\xi_g = \xi_g$. However, including ξ_- means that the other derivatives are taken at fixed $\xi_- = 0$, ie on the physical surface, and ξ_+ is the physical anisotropy ξ .